

Emergence and Localisation of Semantic Role Circuits in LLMs

Nura Aljaafari¹, Danilo S. Carvalho³, André Freitas^{1,2,3}

¹ Department of Computer Science, University of Manchester, United Kingdom

² Idiap Research Institute, Switzerland

³ National Biomarker Centre, CRUK-MI, Univ. of Manchester, United Kingdom

{firstname.lastname}@manchester.ac.uk

Abstract

Despite displaying semantic competence, large language models’ internal mechanisms that ground abstract semantic structure remain insufficiently characterised. We propose a method integrating role-cross minimal pairs, temporal emergence analysis, and cross-model comparison to study how LLMs implement semantic roles. Our analysis uncovers: (i) highly concentrated circuits (89–94% attribution within ≤ 28 nodes); (ii) gradual structural refinement rather than phase transitions, with larger models sometimes bypassing localised circuits; and (iii) moderate cross-scale conservation (24–59% component overlap) alongside high spectral similarity. These findings suggest that LLMs form compact, causally isolated mechanisms for abstract semantic structure, and these mechanisms exhibit partial transfer across scales and architectures.

1 Introduction

Do LLMs develop abstract, causally functional representations of semantic structure? Large language models (LLMs) exhibit localised circuits for factual recall (Goldowsky-Dill et al., 2023a; Meng et al., 2022), arithmetic (Conmy et al., 2023; Stolfo et al., 2023), and logical reasoning (Kim et al., 2025). However, it remains unclear whether such mechanisms extend to the *abstract relational semantic structure* that underlies natural language understanding.

Current mechanistic studies often focus on specialised algorithmic behaviours in trained models (e.g., induction heads, copying, factual associations (Meng et al., 2022; Kissane et al., 2024)), leaving two central gaps in our understanding of semantic representations in LLMs.

First, abstract semantic structure. Semantic roles (e.g., AGENT, THEME, INSTRUMENT) formalise predicate–argument abstractions that generalise across surface forms and syntactic realisations

(Fillmore, 1976). Formally, a semantic role r associates a predicate p and argument position i with a thematic relation: for instance, in “*The children played in the garden*”, the LOCATION role links *garden* to the playing event whether expressed as “*in the garden*”, “*at the garden*”, or “*outside in the garden*” (see Appendix A for a fuller formalisation). From a mechanistic perspective, such predicate–argument binding requires integrating information across tokens and abstracting away from local surface cues, unlike behaviours explained by positional heuristics or lexical templates. Whether LLMs implement this binding through *causally functional circuits* thus remains an open question.

Second, temporal emergence. Most circuit analyses examine only final checkpoints, obscuring when semantic mechanisms arise, stabilise, and become computationally indispensable. Given evidence that several behaviours emerge through sharp transitions (e.g., in-context learning, algorithmic generalisation (Wei et al., 2022; Nanda et al., 2023; He et al., 2024)), it is unclear whether semantic-role circuits likewise appear abruptly or gradually consolidate. Understanding this timeline is important both for training-time interventions (Aljaafari et al., 2025; Cheng et al., 2024) and for explaining how syntactic and semantic abstractions co-develop. To address these questions, we introduce **COMPASS** (Compositional Predicate–Argument Semantic Structure; Fig. 1), a causal–temporal methodology that combines edge-attribution patching (Hanna et al., 2024) with training-time circuit tracking¹. It studies predicate–argument binding using role-cross minimal pairs, disentangles the formation of circuit structure from its functional engagement, and evaluates the transferability of role circuits across model scales. We apply COMPASS to the Pythia (14M–1B) and LLaMA-1B

¹Supporting code and datasets are available at a public repository < anonymised url >

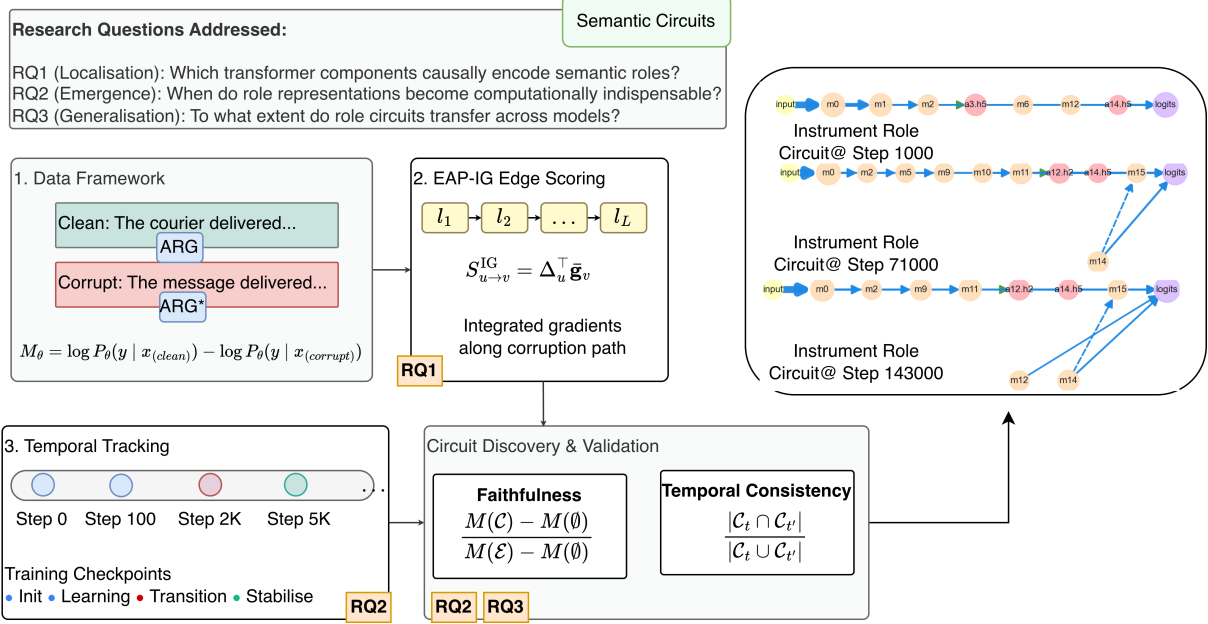


Figure 1: COMPASS methodology. It extracts and tracks the circuits that mediate semantic-role behaviour in LLMs, revealing where role-specific computation occurs and how it develops over training. (1) Role-cross minimal pairs isolate predicate–argument binding. (2) EAP-IG identifies edges whose interventions affect role predictions, producing sparse, causally functional subgraphs. (3) Temporal analysis follows these subgraphs across checkpoints to determine when their structure stabilises and when they become computationally indispensable.

model families to answer:

- **RQ1 (Localisation):** Which model components causally encode semantic roles?
- **RQ2 (Emergence):** When do these circuits become computationally indispensable?
- **RQ3 (Generalisation):** To what extent do role circuits transfer across model scales and architectures?

Across four roles (BENEFICIARY, INSTRUMENT, LOCATION and TIME), we find that role-binding circuits localise to compact sets of attention heads and MLPs, and that larger models reuse similar components while wiring them differently. The results also indicate that predicate–argument binding emerges through *gradual refinement* rather than sudden reorganisation. Circuit presence does not guarantee immediate functional use: models appear to allocate semantic capacity early and exploit it only later. By demonstrating causally determined, functional circuits for shallow semantic structure, our method provides mechanistic evidence that LLMs acquire structured semantic representations and offers new avenues for targeted circuit editing and training-time intervention.

Contributions. We summarise our contributions as: (i) introduce COMPASS, a causal–temporal

method for discovering and tracking semantic-role circuits in LLMs; (ii) show that semantic-role information concentrates in small sets of components whose structural organisation stabilises before becoming functionally indispensable; and (iii) demonstrate partial cross-scale and cross-architecture transfer of these circuits between Pythia (14M–1B) and LLaMA-1B.

2 Related Work

Mechanistic Interpretability and Circuit Discovery. Mechanistic interpretability seeks to reverse-engineer the computations of neural networks (Bereska and Gavves, 2024). Foundational work analysed how attention heads, MLPs, and residual streams implement algorithms (Elhage et al., 2021), leading to discoveries such as induction heads (Olsesson et al., 2022) and circuits for task-specific behaviours (Wang et al., 2022; Conmy et al., 2023). Causal intervention methods form the core of modern circuit analysis: activation patching tests causal effects by swapping activations (Meng et al., 2022), while gradient-based variants such as Attribution Patching (AtP) (Nanda, 2023; Syed et al., 2024) improve scalability but suffer from gradient saturation. AtP* (Kramár et al., 2024) introduces architectural fixes, including gradient dropout and QK decom-

position. More recently, Edge Attribution Patching (EAP) (Hanna et al., 2024) attributes causal influence to individual attention edges, and EAP-IG mitigates saturation effects via Integrated Gradients, offering high faithfulness for fine-grained circuit analysis.

Parallel lines of work seek to disentangle polysemantic features. Sparse Autoencoders (SAEs) extract monosemantic latent features from superimposed representations (Templeton et al., 2024; Bricken et al., 2023), with applications to scripts and relational knowledge (Deng et al., 2025). Transcoders (Dunefsky et al., 2024) approximate component-level transformations via sparse bottlenecks, and attribution graphs (Ameisen et al., 2025) visualise feature interactions using surrogate models. However, surrogate-based approaches introduce reconstruction errors and do not guarantee causal necessity (Gao et al., 2025; Kantamneni et al., 2025). For studying the emergence of semantic circuits across training, methods that operate directly on the original model are required.

Training Dynamics and Compositional Emergence. Transformers often acquire new capabilities through sharp transitions in training dynamics, including grokking-style shifts from memorisation to generalisation (Power et al., 2021; Nanda et al., 2023; Aljaafari et al., 2025) and phase changes in in-context learning (Wei et al., 2022). Recent work also shows that linguistic structure develops progressively: subspaces associated with syntax and semantics become more coherent over training (Müller-Eberstein et al., 2023), and task-specific circuits such as IOI or subject–verb agreement emerge in coordinated phases (Tigges et al., 2024). However, most such analyses rely on probing or scalar metrics, leaving open whether these transitions reflect the emergence of causally functional circuits. To the best of our knowledge, no prior work combines causal circuit localisation with systematic temporal tracking of compositional semantic representations across training and model scale.

Semantic Understanding in Neural Language Models. While transformers achieve strong Semantic Role Labelling (SRL), classifying predicates and argument roles within sentences (Chen et al., 2025), most work examines their accuracy rather than internal mechanisms. Probing studies suggest a hierarchical organisation of linguistic knowledge, lexical features in lower layers, syntax in mid layers, semantics in higher layers (Tenney

et al., 2019; Hewitt and Manning, 2019). However, probing reveals only linear separability, not causal involvement (Caucheteux et al., 2021; Conia and Navigli, 2022). Circuit-level interpretability has mapped concrete behaviours such as IOI (Wang et al., 2022), but has not addressed whether transformers implement causally functional circuits for abstract predicate–argument relations, motivating our focus on semantic-role mechanisms.

Method Positioning. Probing scales efficiently but lacks causal grounding; intervention methods such as path patching (Goldowsky-Dill et al., 2023b) and causal scrubbing (Chan et al., 2022) provide strong guarantees but become computationally prohibitive across many checkpoints. Surrogate-based approaches (SAEs, transcoders) introduce reconstruction artefacts that hinder temporal and cross models comparisons. We therefore employ EAP-IG (Hanna et al., 2024), which provides path-specific causal attribution directly on the original model. We extends EAP-IG to a temporal setting, enabling causal analysis of when semantic-role circuits form, stabilise, and become functionally engaged across training and scale. A detailed comparison of interpretability methods is provided in Appendix G.

3 Methodology

3.1 Semantic Role Circuits

Computational graph representation. Following Hanna et al. (2024), we view transformer computation as a directed acyclic graph $\mathcal{G} = (\mathcal{V}, \mathcal{E})$ where nodes $u \in \mathcal{V}$ correspond to module outputs $u = (\text{type}, \ell, h, i)$ with $\text{type} \in \{\text{AttnHead}, \text{MLP}\}$, layer ℓ , head h (or $h = \emptyset$ for MLPs), and position i . Each u outputs an activation $\mathbf{z}_u \in \mathbb{R}^{d_{\text{model}}}$ to the residual stream, and edges $(u \rightarrow v) \in \mathcal{E}$ denote residual connections.

Task: Role-conditioned continuation. To investigate predicate–argument binding, we adopt a role-conditioned continuation task grounded in frame semantics (Fillmore, 1976) and PropBank-style role inventories (Palmer et al., 2005). The core idea is to vary the *role-indicating scaffold* (e.g., a prepositional phrase) while keeping the predicate and argument fillers fixed. If models represent abstract semantic roles, this behaviour should be mediated by **localised role circuits** $\mathcal{C}^{(r)}$ that map role-indicating scaffolds to role-appropriate continuations. We therefore construct **role-cross mini-**

mal pairs that differ only in the scaffold, enabling isolation of role-specific behaviour. For example:

“The courier delivered the package to the”
 → GOAL: “office”
 “The courier delivered the package with the”
 → INSTRUMENT: “truck”

Pairs use single-token role fillers and enforce **token parity** ($|\text{toks}(x^{(r)})| = |\text{toks}(x^{(s)})|$) to allow us to construct genuine minimal pairs. We additionally retain only items for which the model predicts the correct continuation in both variants, ensuring that any discovered circuits reflect functionally active behaviour (Appendix B).

Evaluation. Task performance uses next-token accuracy:

$$\text{CNP-Acc} = \mathbb{E}_{(x^{(r)}, y^{(r)})} \left[\mathbb{1} \left[y^{(r)} = \arg \max_v P_\theta(v | x^{(r)}) \right] \right] \quad (1)$$

Circuit attribution uses the negative log-probability of the role-appropriate target as the loss:

$$\mathcal{L}_{\text{CNP}}(x^{(r)}, y^{(r)}) = -\log P_\theta(y^{(r)} | x^{(r)}), \quad (2)$$

and EAP-IG attributes this loss to edges to identify components supporting role-appropriate predictions.

3.2 COMPASS: Causal-Temporal Circuit Discovery

COMPASS integrates causal localisation with temporal tracking to recover role circuits $\mathcal{C}^{(r)}$ that exhibit (i) causal necessity, ablating $\mathcal{C}^{(r)}$ reduces task performance; (ii) structural sparsity, $|\mathcal{C}^{(r)}| \ll |\mathcal{E}|$; and (iii) temporal stability, persistent structure after emergence. It also identifies emergence times $(\hat{t}_c, t_{\text{cons}})$ characterising when circuits become functional. The procedure has three phases (full details in Appendix E).

Phase 1: Causal localisation via EAP-IG. For each role pair $(x^{(r)}, x^{(s)})$, EAP-IG (Hanna et al., 2024) computes edge scores by approximating their causal contribution to \mathcal{L}_{CNP} :

$$S_{u \rightarrow v}^{\text{IG}} = \Delta_u^\top \bar{\mathbf{g}}_v, \quad \text{where } \Delta_u = \mathbf{z}_u^{(r)} - \mathbf{z}_u^{(s)}, \quad (3)$$

and $\bar{\mathbf{g}}_v$ averages gradients along an IG interpolation path with $\alpha_k = k/m$ ($m=5$). We normalise by

total mass:

$$\tilde{S}_{u \rightarrow v}^{\text{IG}} = S_{u \rightarrow v}^{\text{IG}} / \sum_{e \in \mathcal{E}} |S_e^{\text{IG}}| \quad (4)$$

and extract the top- $K=200$ edges by $|\tilde{S}_{u \rightarrow v}^{\text{IG}}|$ at each checkpoint t to define $\mathcal{C}_t^{(r)}$. This threshold balances faithfulness saturation with interpretability. Node importance is induced from incident edge mass:

$$\text{Importance}_t^{(r)}(\ell, h) = \sum_{\substack{(u \rightarrow v) \in \mathcal{C}_t^{(r)} \\ v \in (\ell, h)}} |\tilde{S}_{u \rightarrow v}^{\text{IG}}|. \quad (5)$$

Full EAP-IG implementation details appear in Appendix C.

Phase 2: Temporal monitoring. At each checkpoint t , we compute causal and structural signals: *Causal signal*: Faithfulness (Mueller et al., 2025) measures how indispensable a circuit is:

$$\text{Faithfulness}_t(\mathcal{C}) = \frac{M_t(\mathcal{C}) - M_t(\emptyset)}{M_t(\mathcal{E}) - M_t(\emptyset)}, \quad (6)$$

where $M_t(\mathcal{C})$ is CNP accuracy when only edges in \mathcal{C} are active (others zeroed), $M_t(\mathcal{E})$ is full-model performance, and $M_t(\emptyset)$ is the null baseline.

Structural signals. Circuit persistence is measured via Jaccard similarity across consecutive checkpoints:

$$\text{Stability}_t(\mathcal{C}) = \frac{|\mathcal{C}_t \cap \mathcal{C}_{t+\delta}|}{|\mathcal{C}_t \cup \mathcal{C}_{t+\delta}|}, \quad (7)$$

along with Top- K node mass and Gini coefficient to quantify sparsification, detailed ablation protocols are in Appendix C.4.

Phase 3: Emergence detection. We define two temporal markers:

Consolidation time t_{cons} : first step where the top- K node set stabilises:

$$t_{\text{cons}} = \min\{t : \text{Stability}_t(\mathcal{C}) \geq 0.6 \text{ for } \geq 2 \text{ steps}\}. \quad (8)$$

Functional transition \hat{t}_c : change-point in faithfulness, estimated by the best-fitting two-segment linear model to $\{\text{Faithfulness}_t(\mathcal{C}_t)\}_{t=0}^T$ via least-squares regression. The change-point maximising explained variance is:

$$\hat{t}_c = \arg \max_t R^2(\text{PiecewiseLinear}(t)), \quad (9)$$

with 95% confidence intervals via bootstrap resampling ($n = 1,000$). Change-point estimation details and sensitivity analyses appear in Appendix C.4.

3.3 Cross-Model Similarity

We assess whether circuits transfer across models by comparing circuit structure and function via graph overlap and spectral geometry.

Structural overlap. Using the top- $K=30$ nodes and edges ranked by $|\tilde{S}|$, we compute Jaccard overlap between models i, j for each role:

$$J(V_i, V_j) = \frac{|V_i \cap V_j|}{|V_i \cup V_j|}, \quad J(E_i, E_j) = \frac{|E_i \cap E_j|}{|E_i \cup E_j|}. \quad (10)$$

All attributions are normalised by total absolute mass before thresholding to ensure comparability across model scales.

Spectral similarity. To compare higher-order circuit geometry, we compute root-mean-square deviation between the smallest $k = 16$ eigenvalues of the edge-weighted Laplacian using top- $K=50$ edges:

$$d_{\text{spec}}(i, j) = \sqrt{\frac{1}{k} \sum_{m=1}^k (\lambda_m^{(i)} - \lambda_m^{(j)})^2}. \quad (11)$$

Smaller d_{spec} indicates similar information-flow geometry despite differing edge sets. Full spectral analysis methods and Laplacian construction appear in Appendix C.4.

4 Experimental Setup

4.1 Models

We select models to satisfy three requirements: (i) dense training checkpoints to trace circuit formation across training, (ii) variation in model scale to assess circuit transferability, and (iii) architectural diversity to distinguish general computational strategies from implementation-specific artefacts. PYTHIA (14M, 410M, 1B; [Biderman et al., 2023](#)) provides full checkpoints from initialisation to convergence, enabling fine-grained analysis of when semantic-role circuits first emerge and consolidate. To test whether these circuits persist beyond a single family, we include LLAMA-1B ([Touvron et al., 2023](#)), which differs in tokenisation, training data, and architectural choices. This pairing separates training-time dynamics (within family) from architectural robustness (across families). Although not intended as an exhaustive model survey, this combination is sufficient to assess whether the mechanisms we identify reflect general training-driven pressures rather than results of a specific implementation.

4.2 Datasets and Experimental Software

We instantiate the role-conditioned continuation task (Sec. 3.1) focusing on four roles: BENEFICIARY, INSTRUMENT, LOCATION, and TIME. These roles are selected to span different types of semantic relations commonly represented in frame-semantic and role-labelling resources: participant roles (BENEFICIARY, INSTRUMENT) and circumstantial roles (LOCATION, TIME). This selection provides variation in lexical and syntactic realisation while keeping the experimental design tractable. Following Sec. 3.1, the generated pairs follow token parity and were filtered to retain only examples where the model correctly predicts the role-appropriate target in both contexts. After filtering with Pythia-1B, we obtain 4740 pairs (≥ 350 per role). Additional roles (GOAL, PATH, SOURCE, TOPIC) are analysed in Appendix F.3, where we show that they display the same qualitative localisation and emergence patterns, supporting the generality of our conclusions. Full construction details, filtering procedures, and dataset statistics are provided in Appendix B, and we also provide software and computation specifications in Appendix D.1.

5 Results

We address three research questions about semantic-role circuits across four roles (BENEFICIARY, INSTRUMENT, LOCATION, TIME) in Pythia (14M, 410M, 1B) and LLaMA-1B. Unless otherwise noted, we report results for PYTHIA-1B. Full results and metric definitions appear in Appendices F and E.

5.1 Localisation of Role Circuits (RQ1)

We find highly localised circuits for all tested roles, with the top 20 nodes capturing 89–94% of attribution mass at convergence (Table 1). Despite this shared sparsity, roles exhibit qualitatively distinct architectures and developmental trajectories.

Circuit architectures vary by role. Causal-flow analysis (Fig. 2) reveals systematic cross-role differences reflecting semantic demands. For example, BENEFICIARY exhibits the most complex developmental trajectory: at step 32 (23 nodes), it recruits moderate early-layer attention (a0.h1, a0.h2, a0.h4–a0.h6) alongside extensive MLP branching. By step 71000 (21 nodes), the circuit reorganises into complex late stage architecture with three distinct value-composition operations (a9.h2+V, a14.h5+V, a15.h5+V), indicating intensive feature extraction.

Role (final step = 143k)	Top–20 mass	Gini (mass)
BENEFICIARY	0.906	0.439
INSTRUMENT	0.917	0.489
LOCATION	0.897	0.519
TIME	0.935	0.468

Table 1: Sparsity statistics for role circuits at convergence (PYTHIA–1B, step 143k). The table reports Top–20 mass (the fraction of attribution carried by the 20 highest-mass nodes) and the corresponding Gini coefficients. All roles exhibit high concentration, indicating that semantic-role computation is mediated by compact subgraphs. Gini values (higher = tighter concentration) show that TIME has the most compact attribution profile, while LOCATION spreads mass more evenly across its top components, reflecting small but systematic differences in circuit concentration across roles.

At convergence (step 143000, 22 nodes), it maintains rich connectivity with six attention heads. In contrast, other roles converge to simpler architectures: TIME achieves mostly MLP implementation by mid-training; INSTRUMENT stabilises to balanced hybrid (20 nodes, 4 heads); LOCATION contracts from mid-training expansion to distributed integration. Further, cross-role comparison of top- K components (Fig. 4) shows consistently low Jaccard overlap, confirming that these architectural patterns correspond to distinct, role-specific subgraphs rather than shared motifs. Full circuit evolution for all eight roles appears in Appendix F.4.

Quantitative localisation. Table 1 summarises sparsity at convergence. All roles show tight concentration, with the top 20 nodes capturing 89–94% of total mass. TIME is the most compact (93.5%), while LOCATION distributes mass slightly more evenly across its top components (Gini = 0.519), reflecting modest differences in how sharply each role concentrates attribution within its circuit.

Roles exhibit distinct developmental trajectories. Temporal analysis (Fig. 3) shows heterogeneous emergence dynamics. BENEFICIARY displays the smoothest progression: faithfulness increases steadily, and edge density rises steadily ($0.09 \rightarrow 0.14$), indicating progressive consolidation into compact circuits. INSTRUMENT starts with high faithfulness (peak $\simeq 2.45$ at step 0), then undergoes a sharp decline and stabilises at lower levels, with edge density dipping before rising, suggesting late consolidation into denser pathways. LOCATION exhibits moderate initial faithfulness with mid-training fluctuations and mild late recov-

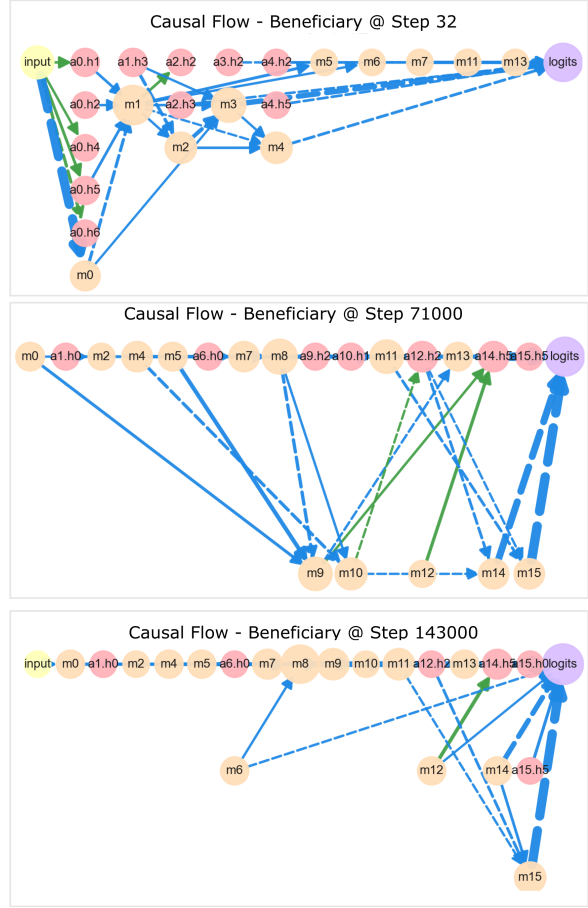


Figure 2: Evolution of the BENEFICIARY circuit across training. The circuit undergoes complex re-organisation from early exploration (step 32) through intensive mid-training feature extraction (step 71000) to its final architecture (step 143000). BENEFICIARY’s delayed structural consolidation ($t_{\text{cons}} = 2,000$) and persistent complexity reflect the computational demands of distinguishing benefactive from alternative role readings. Edge colour encodes operation type (blue: residual flow; green: value-composition; dashed: negative); edge width is proportional to attribution magnitude.

ery, while edge density grows steadily, consistent with gradual strengthening of connectivity. TIME shows the strongest non-monotonicity: faithfulness begins high ($\simeq 2.0$), drops sharply, and partially recovers. Circuit size decreases early but re-expands in the final 70K steps, and edge density peaks highest of any role ($\simeq 0.20$ around step 70k) before settling, yielding a distinctive “expand–contract” pattern.

Key findings. **(i) Highly concentrated circuits with role-specific structure.** All roles converge to compact circuits (89–94% mass in 20 nodes; Table 1) but exhibit distinct patterns: INSTRUMENT uses bridge-augmented MLP spines, TIME main-

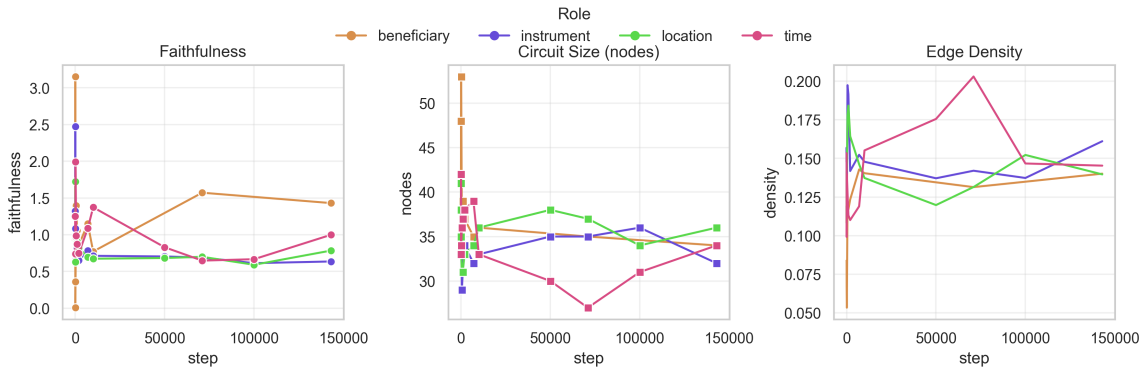


Figure 3: Structural and functional dynamics of role circuits across training. Faithfulness (left) shows pronounced role-dependent volatility, with early peaks and mid-training drops, indicating that circuit usefulness does not increase monotonically. In contrast, structural metrics evolve more smoothly: circuit size (middle) contracts gradually, and edge density (right) rises or stabilises over time. These trends show that circuit structure consolidates early and steadily, while functional engagement remains variable across roles.

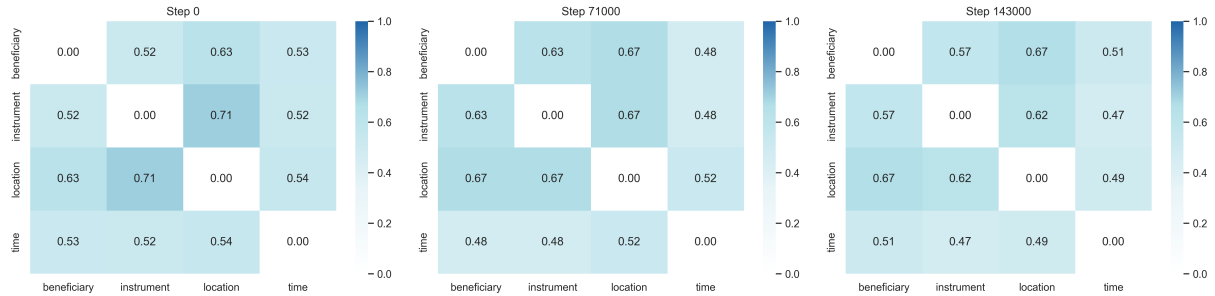


Figure 4: Cross-role overlap of high-importance components over training (PYTHIA-1B). Each heatmap shows the Jaccard similarity between the nodes for different roles at three sample training stages. Overlap remains consistently low, indicating that roles recruit largely distinct component sets. This specialisation strengthens over training, supporting the view that role circuits differentiate rather than collapse into a shared mechanism.

tains mid-layer cores, LOCATION densifies gradually, and BENEFICIARY streamlines progressively. Low cross-role overlap (Fig. 4) confirms strong component specialisation. **(ii) Continuous refinement, not discrete transitions.** Structural metrics (Top- K mass, edge density, circuit size; Fig. 3) evolve smoothly throughout training. Even roles with large functional swings (INSTRUMENT, TIME) show gradual consolidation, indicating incremental optimisation rather than abrupt phase shifts. **(iii) Structure–function dissociation.** Faithfulness is often non-monotonic (e.g., TIME drops then recovers) even as sparsity increases. Circuits can be structurally well-formed yet temporarily under-utilised, challenging assumptions that presence implies consistent engagement. **(iv) Role-specific stabilisation timelines.** Roles consolidate at different rates: INSTRUMENT and LOCATION stabilise earliest (high Top- K Jaccard by 10K steps), TIME stabilises later and less strongly, and BENEFICIARY consolidates slowly but consistently.

5.2 Emergence Dynamics (RQ2)

We find that role-binding circuits emerge via *continuous refinement* rather than discrete phase transitions. Roles become causally indispensable early in training (within 0–128 steps), but structural consolidation unfolds over tens of thousands of steps, producing pronounced *structure–function dissociation*.

Early indispensability with role-specific emergence. Roles become causally indispensable at heterogeneous stages (Table 2). TIME circuits are indispensable from initialisation ($t_{\text{ind}} = 0$), INSTRUMENT by step 32, and LOCATION by step 128. BENEFICIARY presents a distinct pattern: the circuit faithfulness improves throughout training, but ablation never exceeds our conservative $\mu + \sigma$ threshold, leaving t_{ind} undefined; the circuit is helpful but not provably necessary under our criterion. This structure–function dissociation (rapid structural consolidation with variable functional engage-

Role	t_{ind} (steps)	t_{cons} (steps)
BENEFICIARY	–	2,000
INSTRUMENT	32	8
LOCATION	128	8
TIME	0	8

Table 2: **Emergence timings for role circuits.** For each role, t_{ind} marks the earliest step where ablation consistently harms performance, and t_{cons} the first point where the circuit’s structure stabilises (Jaccard ≥ 0.6 over two steps). All roles consolidate within $\sim 2k$ steps, but indispensability varies widely, with some circuits becoming necessary immediately and others only much later or not at all.

ment for most roles; delayed consolidation without strict necessity for Beneficiary) likely reflects differences in cue salience, distributional frequency, and the computational complexity required for disambiguation. We study circuits heterogeneity and temporal instability in Appendix F4, which provides detailed architectural analyses among roles circuits.

Continuous sparsification without phase transitions. Piecewise linear regression on Top- K mass trajectories yields change-point estimates with bootstrap confidence intervals spanning multiple orders of magnitude (Table 3). BENEFICIARY, INSTRUMENT, and LOCATION share $\hat{t}_c = 512$ with CIs [32, 10,000], [8, 71,000], and [8, 7,000], respectively; TIME shows $\hat{t}_c = 7,000$ with CI [32, 50,000]. These intervals are far too wide to localise any discrete transition: structural sparsification evolves continuously, *contrasting with grokking* (Power et al., 2021; Nanda et al., 2023), where change-points are precise and abrupt. Structural metrics evolve smoothly (Fig. 3): Top- K mass reaches ≈ 0.90 by step 1k and then saturates gradually; edge density increases steadily, with BENEFICIARY and INSTRUMENT showing monotonic growth and LOCATION/TIME exhibiting mild “expand–contract” patterns as weak connections are pruned. Final concentration is extreme: Top-20 nodes capture 89.7–93.5% of mass (Table 4), with 95% coverage in just 22–28 nodes.

Structure–function dissociation. Although structural metrics evolve smoothly, faithfulness trajectories exhibit pronounced non-monotonicity (Fig. 3, left). BENEFICIARY crashes early then recovers; INSTRUMENT and LOCATION peak early then plateau; TIME shows the sharpest mid-training crashes and late recovery. This *functional*

Role	\hat{t}_c (steps)	95% CI
BENEFICIARY	512	[32, 10,000]
INSTRUMENT	512	[8, 71,000]
LOCATION	512	[8, 7,000]
TIME	7,000	[32, 50,000]

Table 3: **Change-point estimates** for *Top- K node mass* obtained via two-segment piecewise linear regression with bootstrap resampling. The extremely wide confidence intervals indicate that structural sparsification evolves gradually and continuously rather than through a discrete phase transition; no statistically localisable break-points appear in the trajectories.

Role	Top-5	Top-10	Top-20	k for 80/90/95%
BENEFICIARY	0.395	0.611	0.906	16 / 20 / 25
INSTRUMENT	0.492	0.688	0.917	14 / 19 / 23
LOCATION	0.483	0.673	0.897	15 / 21 / 25
TIME	0.386	0.635	0.935	15 / 18 / 22

Table 4: **Final-step concentration of role circuits.** Top- K mass and coverage thresholds reveal that each role exhibits a sharply concentrated attribution distribution. The small k values required to cover most of mass show that a limited subset of nodes drives the majority of the circuit’s computation, with role-to-role variation reflecting consistent but distinct concentration patterns.

volatility despite structural stability shows that circuits can be structurally present while being temporarily underutilised. Structural consolidation precedes functional indispensability by many of steps (Table 2: $t_{\text{cons}} = 8$ vs. $t_{\text{ind}} = 32\text{--}128$), demonstrating that *circuit presence does not guarantee circuit engagement*.

Key findings. **(i) Continuous refinement throughout training.** Structural metrics (Top- K mass, edge density, circuit size) evolve smoothly with no discrete transitions; wide change-point CIs indicate no identifiable phase shifts. **(ii) Early indispensability, prolonged consolidation.** Roles become indispensable within 0–128 steps, but structural refinement continues for 140K+ steps. Structure stabilises early, but attribution mass continues to redistribute. **(iii) Structure–function dissociation and delayed engagement.** Circuits stabilise structurally ($t_{\text{cons}} = 8$) many steps before becoming functionally indispensable ($t_{\text{ind}} = 32\text{--}128$). Faithfulness shows crashes and recoveries even as sparsity increases, illustrating that *circuit presence does not mean circuit engagement*. **(iv) Role-specific developmental trajectories.** Despite shared qualitative patterns (continuous sparsification, early consolidation), roles show

distinct functional dynamics: **BENEFICIARY** recovers after an early crash, **LOCATION** plateaus mid-training, **INSTRUMENT** peaks then declines, and **TIME** exhibits severe mid-training instability.

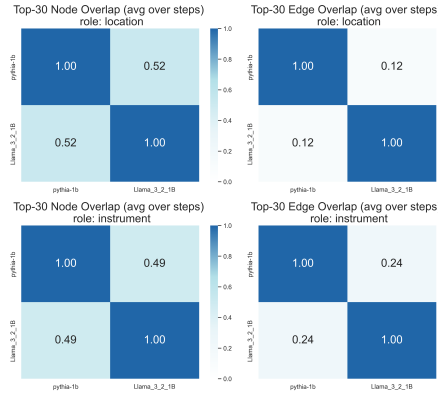


Figure 5: Cross-family correspondence for Location (top) and Instrument (bottom). Average node-(left) and edge-level (right) overlaps between PYTHIA-1B and LLAMA-1B. Node sets align substantially more than edges, suggesting shared component selection but model-specific routing.

5.3 Cross-Scale and Cross-Family Generalisation (RQ3)

We find moderate structural conservation (24–59% node overlap) across scales and model families. Models converge on shared *functional vocabularies* (high-importance components) while implementing divergent *routing patterns*: component reuse exceeds connection reuse by $\sim 2:1$. Spectral analysis reveals functional alignment despite topological divergence, with small eigenvalue distances (< 0.02) coexisting with 76–88% edge mismatch.

Cross-scale correspondence within Pythia. Node-level overlap increases with scale proximity (Table 5): $14M \leftrightarrow 410M$ yields $J_V = 0.24$, $14M \leftrightarrow 1B$ reaches $J_V = 0.29$, and $410M \leftrightarrow 1B$ achieves $J_V = 0.44$, the strongest within-family match. Edge-level overlap remains low ($J_E \approx 0.12\text{--}0.15$), indicating that models reuse similar high-importance nodes but wire them differently. Spectral distances decrease with scale ($d_{\text{spec}} = 0.12 \rightarrow 0.11 \rightarrow 0.01$), suggesting progressive geometric refinement: larger models realise similar information-flow patterns with increasingly aligned connectivity. This pattern reflects shared training conditions (corpus, token ordering, optimiser) and architectural continuity within the Pythia family.

Model pair	Node J.	Edge J.	d_{spec}
PYTHIA-14M \leftrightarrow PYTHIA-410M	0.24	0.12	0.12
PYTHIA-14M \leftrightarrow PYTHIA-1B	0.29	0.14	0.11
PYTHIA-410M \leftrightarrow PYTHIA-1B	0.44	0.15	0.01
PYTHIA-1B \leftrightarrow LLAMA-1B	0.59	0.17	0.02

Table 5: Cross-scale and cross-family similarity of role circuits. Node-level overlap increases with model scale, while edge-level overlap remains low, signifying that models tend to reuse similar components while reconfiguring them differently. The cross-family comparison ($PYTHIA-1B \leftrightarrow LLAMA-1B$) shows the highest node overlap, suggesting that key components are preserved across architectures even when connectivity patterns diverge. Values report median Top- K Jaccard ($K=30$) and spectral distance (d_{spec}) computed from the lowest $k=20$ Laplacian eigenvalues. Lower d_{spec} indicates higher functional similarity.

Cross-family correspondence: PYTHIA-1B vs. LLAMA-1B. The cross-family comparison exhibits the *highest node overlap* in our study ($J_V = 0.59$), exceeding even the closest within-Pythia pair ($410M \leftrightarrow 1B$: $J_V = 0.44$). This suggests that architectural constraints at the 1B scale bias both models toward similar component sets for role processing, despite different pretraining corpora (Pile vs. mixed web data) and architectural choices (grouped-query attention, RoPE vs. learned positional encodings). However, edge-level overlap remains modest ($J_E = 0.17$), and spectral distance ($d_{\text{spec}} = 0.02$) slightly exceeds the best within-family match ($d_{\text{spec}} = 0.01$ for $410M \leftrightarrow 1B$). This “shared components, divergent wiring” pattern indicates that models converge on a common functional vocabulary (which MLPs and heads participate) while implementing distinct routing schemas shaped by architectural and training differences.

Role-specific patterns. Per-role analysis (Fig. 5) reveals heterogeneous transferability. **INSTRUMENT** shows the strongest spectral consistency ($d_{\text{spec}} < 0.01$ for $410M \leftrightarrow 1B$), indicating highly transferable motifs; its bridge-augmented MLP spines (RQ1) replicate reliably across scales. **LOCATION** displays the largest divergence, especially at small scales ($J_V \approx 0.18\text{--}0.22$ for $14M$ comparisons), consistent with its distributed, attention-mediated architecture (RQ1) that may require scale-dependent reorganisation. **TIME** exhibits moderate node overlap but strong spectral alignment ($d_{\text{spec}} \approx 0.01$), implying similar information-flow geometry realised through different topological

configurations. BENEFICIARY shows intermediate patterns, reflecting its progressive consolidation trajectory (RQ2). Across all roles, node-level overlap consistently exceeds edge-level overlap by $\sim 2\text{--}2.5 \times$, reinforcing that component reuse dominates connection reuse. Full per-role results are in Appendix F.

Key findings. **(i) Moderate structural conservation across scales and families.** High-importance nodes show 24–59% overlap. Cross-family correspondence (PYTHIA-1B \leftrightarrow LLAMA-1B: 59%) exceeds the strongest within-family pairing (410M \leftrightarrow 1B: 44%). This indicates circuits reflect both task demands and model-specific factors, neither fully architecture-agnostic nor purely model-bound. **(ii) Component reuse exceeds connection reuse.** Node-to-edge overlap ratios show models converge on shared functional vocabularies (which components matter) while diverging in routing structure (how they connect). Circuits thus exhibit constrained diversity: common primitives, varied implementations. **(iii) Spectral alignment despite topological divergence.** Small spectral distances ($d_{\text{spec}} < 0.02$) coexist with large edge differences (76–88%), indicating that models realise similar information-flow geometry via distinct connectivity patterns. **(iv) Scale-dependent refinement within families.** Spectral distance decreases monotonically across PYTHIA scales, suggesting that larger models progressively align their flow geometry. The cross-family increase to $d_{\text{spec}} = 0.02$ reflects architectural differences (e.g., attention variants, positional encodings) that shape circuit realisation despite shared task demands.

6 Discussion

Synthesis across RQs. Our analyses reveal complementary aspects of semantic-role circuits. *RQ1* showed that role information localises into compact, sparsely concentrated subgraphs with role-specific architectural motifs. *RQ2* demonstrated that these circuits emerge gradually: indispensability often appears early, but sparsity, density, and attribution patterns evolve smoothly while faithfulness exhibits role-dependent volatility. *RQ3* found partial cross-scale and cross-family conservation, with models reusing similar high-importance components but wiring them differently.

Mechanistic interpretation. Semantic-role circuits appear to arise through prolonged optimi-

sation rather than discrete phase transitions. Although functional competence often emerges early, the underlying computational substrate continues to be reweighted and reorganised. Gradients favour whichever pathways currently yield good predictions, while architectural constraints and implicit regularisation gradually funnel computation into compact motifs (e.g., MLP spines supported by attention bridges). The heterogeneity across roles further indicates that circuits are not simply “switched on” and then fixed: high-importance nodes may stabilise structurally long before the model consistently relies on them. Cross-scale patterns reinforce this view: models share a *functional vocabulary*, the same components tend to matter—but instantiate it through diverse *routing schemes* shaped by scale and architectural details.

Linguistic perspective. From a linguistic standpoint, these circuits approximate role–filler bindings central to the semantics of predicate–argument structure (*who did what to whom, when, with what*). Their localisation to compact, causally engaged subgraphs suggests that models encode such relations via partially modular mechanisms rather than diffuse token-level heuristics. The partial cross-family convergence, despite different architectures, mirrors a familiar observation in formal semantics: semantic roles behave like typed relational predicates whose abstract relational types remain stable even when different formalisms realise them through distinct derivational routes. By analogy, our results point to shared representational primitives combined with architecture-dependent wiring.

Implications and significance. Most mechanistic interpretability work investigates narrow behaviours or single checkpoints. Our framework extends this along three axes: (i) **temporal**, by identifying when circuits first appear and when they become functionally engaged; (ii) **cross-scale**, by assessing whether mechanisms persist across model sizes and model families; and (iii) **semantic**, by analysing predicate–argument structure rather than lexical cues or isolated behavioural tasks. The presence of compact, causally functional circuits for our studied semantic structure suggests that LLMs do more than memorise surface co-occurrences. Moreover, partial cross-scale and cross-family transfer indicates that these mechanisms reflect underlying task structure rather than idiosyncratic artifacts, supporting the view that mechanistic interpretability can uncover general

computational principles. For safety and alignment, the ability to *localise* and *track* abstract semantic mechanisms enables targeted interventions: if specific subgraphs mediate undesirable behaviours, edits can in principle act directly on those circuits rather than global retraining. The heterogeneous emergence timelines we observe also suggest that different semantic capabilities stabilise at different stages, raising the possibility of steering training curricula or early-stopping strategies to emphasise or suppress particular semantic behaviours.

Limitations and future work. Our study focuses on English and a subset of roles; whether similar circuits arise in typologically diverse languages or for richer role inventories remains unknown. The wide change-point confidence intervals reflect the smoothness of structural trajectories rather than methodological noise, but more sensitive emergence metrics (e.g., information-theoretic or curvature-based) may yield finer resolution. Finally, we analyse decoder-only architectures; whether encoder–decoder models exhibit analogous reuse patterns remains an open question. Future work should extend this analysis to multilingual and multimodal models, study interactions between semantic-role circuits and mechanisms for syntax or coreference, and test whether analogous emergence patterns appear for other semantic abstractions such as quantification, modality, or negation.

References

- Nura Aljaafari, Danilo S Carvalho, and André Freitas. 2025. Trace: Training and inference-time interpretability analysis for language models. *arXiv preprint arXiv:2507.03668*.
- Emmanuel Ameisen, Jack Lindsey, Adam Pearce, Wes Gurnee, Nicholas L. Turner, Brian Chen, Craig Citro, David Abrahams, Shan Carter, Basil Hosmer, Jonathan Marcus, Michael Sklar, Adly Templeton, Trenton Bricken, Callum McDougall, Hoagy Cunningham, Thomas Henighan, Adam Jermyn, Andy Jones, and 8 others. 2025. Circuit tracing: Revealing computational graphs in language models. *Transformer Circuits Thread*.
- Collin F. Baker, Charles J. Fillmore, and John B. Lowe. 1998. The berkeley frameNet project. In *Proceedings of the 36th Annual Meeting of the Association for Computational Linguistics and 17th International Conference on Computational Linguistics - Volume 1*, ACL ’98/COLING ’98, page 86–90, USA. Association for Computational Linguistics.
- Leonard Bereska and Stratis Gavves. 2024. Mechanistic interpretability for AI safety - a review. *Transactions on Machine Learning Research*. Survey Certification, Expert Certification.
- Stella Biderman, Hailey Schoelkopf, Quentin Gregory Anthony, Herbie Bradley, Kyle O’Brien, Eric Hallahan, Mohammad Aflah Khan, Shivanshu Purohit, USVSN Sai Prashanth, Edward Raff, and 1 others. 2023. Pythia: A suite for analyzing large language models across training and scaling. In *International Conference on Machine Learning*, pages 2397–2430. PMLR.
- Trenton Bricken, Adly Templeton, Joshua Batson, Brian Chen, Adam Jermyn, Tom Conerly, Nick Turner, Cem Anil, Carson Denison, Amanda Askell, Robert Lasenby, Yifan Wu, Shauna Kravec, Nicholas Schiefer, Tim Maxwell, Nicholas Joseph, Zac Hatfield-Dodds, Alex Tamkin, Karina Nguyen, and 6 others. 2023. Towards monosemanticity: Decomposing language models with dictionary learning. *Transformer Circuits Thread*.
- Charlotte Caucheteux, Alexandre Gramfort, and Jean-Remi King. 2021. Disentangling syntax and semantics in the brain with deep networks. In *International conference on machine learning*, pages 1336–1348. PMLR.
- Lawrence Chan, Adrià Garriga-Alonso, Nicholas Goldwosky-Dill, Ryan Greenblatt, Jenny Nitishinskaya, Ansh Radhakrishnan, Buck Shlegeris, and Nate Thomas. 2022. Causal scrubbing, a method for rigorously testing interpretability hypotheses. *AI Alignment Forum*. <https://www.alignmentforum.org/posts/JvZhhzycHu2Yd57RN/causal-scrubbing-a-method-for-rigorously-testing>.
- Huiyao Chen, Meishan Zhang, Jing Li, Min Zhang, Lilja Øvreliid, Jan Hajič, and Hao Fei. 2025. Semantic role labeling: A systematical survey. *Preprint*, arXiv:2502.08660.
- Ning Cheng, Zhaohui Yan, Ziming Wang, Zhijie Li, Jiaming Yu, Zilong Zheng, Kewei Tu, Jinan Xu, and Wenjuan Han. 2024. Potential and limitations of llms in capturing structured semantics: A case study on srl. In *Advanced Intelligent Computing Technology and Applications*, pages 50–61, Singapore. Springer Nature Singapore.
- Simone Conia and Roberto Navigli. 2022. Probing for predicate argument structures in pretrained language models. In *Proceedings of the 60th Annual Meeting of the Association for Computational Linguistics (Volume 1: Long Papers)*, pages 4622–4632, Dublin, Ireland. Association for Computational Linguistics.
- Arthur Conmy, Augustine Mavor-Parker, Aengus Lynch, Stefan Heimersheim, and Adrià Garriga-Alonso. 2023. Towards automated circuit discovery for mechanistic interpretability. *Advances in Neural Information Processing Systems*, 36:16318–16352.

- Ruixuan Deng, Xiaoyang Hu, Miles Gilberti, Shane Storks, Aman Taxali, Mike Angstadt, Chandra Sripada, and Joyce Chai. 2025. Sparse feature coactivation reveals composable semantic modules in large language models. *arXiv preprint arXiv:2506.18141*.
- Jacob Dunefsky, Philippe Chlenski, and Neel Nanda. 2024. [Transcoders find interpretable LLM feature circuits](#). In *The Thirty-eighth Annual Conference on Neural Information Processing Systems*.
- Nelson Elhage, Neel Nanda, Catherine Olsson, Tom Henighan, Nicholas Joseph, Ben Mann, Amanda Askell, Yuntao Bai, Anna Chen, Tom Conerly, and 1 others. 2021. A mathematical framework for transformer circuits. *Transformer Circuits Thread*, 1(1):12.
- Charles J Fillmore. 1976. Frame semantics and the nature of language. *Annals of the New York Academy of Sciences*, 280(1):20–32.
- Leo Gao, Tom Dupre la Tour, Henk Tillman, Gabriel Goh, Rajan Troll, Alec Radford, Ilya Sutskever, Jan Leike, and Jeffrey Wu. 2025. [Scaling and evaluating sparse autoencoders](#). In *The Thirteenth International Conference on Learning Representations*.
- Nicholas Goldowsky-Dill, Chris MacLeod, Lucas Jun Koba Sato, and Aryaman Arora. 2023a. [Localizing model behavior with path patching](#). *CoRR*, abs/2304.05969.
- Nicholas Goldowsky-Dill, Chris MacLeod, Lucas Jun Koba Sato, and Aryaman Arora. 2023b. [Localizing model behavior with path patching](#). *ArXiv*, abs/2304.05969.
- Michael Hanna, Sandro Pezzelle, and Yonatan Belinkov. 2024. [Have faith in faithfulness: Going beyond circuit overlap when finding model mechanisms](#). In *ICML 2024 Workshop on Mechanistic Interpretability*.
- Tianyu He, Darshil Doshi, Aritra Das, and Andrey Gromov. 2024. Learning to grok: Emergence of in-context learning and skill composition in modular arithmetic tasks. *Advances in Neural Information Processing Systems*, 37:13244–13273.
- John Hewitt and Christopher D. Manning. 2019. [A structural probe for finding syntax in word representations](#). In *North American Chapter of the Association for Computational Linguistics*.
- Daniel Jurafsky and James H. Martin. 2025. *Speech and Language Processing: An Introduction to Natural Language Processing, Computational Linguistics, and Speech Recognition, with Language Models*, 3rd edition. Online manuscript released August 24, 2025.
- Subhash Kantamneni, Joshua Engels, Senthooran Rajamanoharan, Max Tegmark, and Neel Nanda. 2025. Are sparse autoencoders useful? a case study in sparse probing. *arXiv preprint arXiv:2502.16681*.
- Geonhee Kim, Marco Valentino, and André Freitas. 2025. Reasoning circuits in language models: A mechanistic interpretation of syllogistic inference. In *Findings of the Association for Computational Linguistics: ACL 2025*, pages 10074–10095.
- Connor Kissane, Robert Krzyzanowski, Arthur Conmy, and Neel Nanda. 2024. [Attention saes scale to gpt-2 small](#). Alignment Forum.
- János Kramár, Tom Lieberum, Rohin Shah, and Neel Nanda. 2024. Atp*: An efficient and scalable method for localizing llm behaviour to components. *arXiv preprint arXiv:2403.00745*.
- Kevin Meng, David Bau, Alex Andonian, and Yonatan Belinkov. 2022. Locating and editing factual associations in gpt. *Advances in neural information processing systems*, 35:17359–17372.
- Aaron Mueller, Atticus Geiger, Sarah Wiegreffe, Dana Arad, Iván Arcuschin, Adam Belfki, Yik Siu Chan, Jaden Fried Fiotto-Kaufman, Tal Haklay, Michael Hanna, Jing Huang, Rohan Gupta, Yaniv Nikankin, Hadas Orgad, Nikhil Prakash, Anja Reusch, Aruna Sankaranarayanan, Shun Shao, Alessandro Stolfo, and 4 others. 2025. [MIB: A mechanistic interpretability benchmark](#). In *Forty-second International Conference on Machine Learning*.
- Max Müller-Eberstein, Rob van der Goot, Barbara Plank, and Ivan Titov. 2023. [Subspace chronicles: How linguistic information emerges, shifts and interacts during language model training](#). In *Findings of the Association for Computational Linguistics: EMNLP 2023*, pages 13190–13208, Singapore. Association for Computational Linguistics.
- Neel Nanda. 2023. Attribution patching: Activation patching at industrial scale. <https://www.neelnanda.io/mechanistic-interpretability/attribution-patching>.
- Neel Nanda, Lawrence Chan, Tom Lieberum, Jess Smith, and Jacob Steinhardt. 2023. [Progress measures for grokking via mechanistic interpretability](#). In *The Eleventh International Conference on Learning Representations*.
- Catherine Olsson, Nelson Elhage, Neel Nanda, Nicholas Joseph, Nova DasSarma, Tom Henighan, Ben Mann, Amanda Askell, Yuntao Bai, Anna Chen, and 1 others. 2022. In-context learning and induction heads. *arXiv preprint arXiv:2209.11895*.
- Martha Palmer, Daniel Gildea, and Paul Kingsbury. 2005. [The proposition bank: An annotated corpus of semantic roles](#). *Comput. Linguist.*, 31(1):71–106.
- Alethea Power, Yuri Burda, Harri Edwards, Igor Babuschkin, and Vedant Misra. 2021. Grokking: Generalization beyond overfitting on small algorithmic datasets. In *ICLR MATH-AI Workshop*.
- Beatrice Santorini and Anthony Kroch. 2007. [The syntax of natural language: An online introduction](#).

Alessandro Stolfo, Yonatan Belinkov, and Mrinmaya Sachan. 2023. [A mechanistic interpretation of arithmetic reasoning in language models using causal mediation analysis](#). In *Conference on Empirical Methods in Natural Language Processing*.

Mukund Sundararajan, Ankur Taly, and Qiqi Yan. 2017. Axiomatic attribution for deep networks. In *International conference on machine learning*, pages 3319–3328. PMLR.

Aaquib Syed, Can Rager, and Arthur Conmy. 2024. [Attribution patching outperforms automated circuit discovery](#). In *Proceedings of the 7th BlackboxNLP Workshop: Analyzing and Interpreting Neural Networks for NLP*, pages 407–416, Miami, Florida, US. Association for Computational Linguistics.

Adly Templeton, Tom Conerly, Jonathan Marcus, Jack Lindsey, Trenton Bricken, Brian Chen, Adam Pearce, Craig Citro, Emmanuel Ameisen, Andy Jones, Hoagy Cunningham, Nicholas L Turner, Callum McDougall, Monte MacDiarmid, C. Daniel Freeman, Theodore R. Sumers, Edward Rees, Joshua Batson, Adam Jermyn, and 3 others. 2024. Scaling monosematicity: Extracting interpretable features from claude 3 sonnet. *Transformer Circuits Thread*.

Ian Tenney, Dipanjan Das, and Ellie Pavlick. 2019. [Bert rediscovers the classical nlp pipeline](#). In *Annual Meeting of the Association for Computational Linguistics*.

Curt Tigges, Michael Hanna, Qinan Yu, and Stella Bierman. 2024. [Llm circuit analyses are consistent across training and scale](#). In *Advances in Neural Information Processing Systems*, volume 37, pages 40699–40731. Curran Associates, Inc.

Hugo Touvron, Thibaut Lavril, Gautier Izacard, Xavier Martinet, Marie-Anne Lachaux, Timothée Lacroix, Baptiste Rozière, Naman Goyal, Eric Hambro, Faisal Azhar, and 1 others. 2023. Llama: Open and efficient foundation language models. *arXiv preprint arXiv:2302.13971*.

Kevin Wang, Alexandre Variengien, Arthur Conmy, Buck Shlegeris, and Jacob Steinhardt. 2022. Interpretability in the wild: a circuit for indirect object identification in gpt-2 small. *arXiv preprint arXiv:2211.00593*.

Jason Wei, Yi Tay, Rishi Bommasani, Colin Raffel, Barret Zoph, Sebastian Borgeaud, Dani Yogatama, Maarten Bosma, Denny Zhou, Donald Metzler, Ed H. Chi, Tatsunori Hashimoto, Oriol Vinyals, Percy Liang, Jeff Dean, and William Fedus. 2022. [Emergent abilities of large language models](#). *Transactions on Machine Learning Research*. Survey Certification.

A Linguistic Background: Predicate–Argument Structure and Thematic Roles

A.1 Predicate–Argument Structure

Predicates, typically verbs, denote events or states and introduce *argument positions* corresponding to event participants ([Santorini and Kroch, 2007](#)). In “*The courier delivered the package to the office with the truck*”, the predicate *deliver* evokes a transfer event with participants such as the actor (*courier*), the transferred entity (*package*), the destination (*office*), and the means (*truck*). These participants may be realised as subjects, objects, or prepositional phrases, but surface form does not uniquely determine semantic function: “with X” may express INSTRUMENT (*with the truck*) or COMITATIVE (*with Mary*), and the same role may occur in different syntactic configurations (e.g., dative alternation: “*give the book to Mary*” vs. “*give Mary the book*”).

A.2 Thematic Roles (θ -Roles)

Thematic roles provide a shallow semantic representation that captures how participants relate to an event ([Fillmore, 1976](#)). Roles such as AGENT, THEME, GOAL, INSTRUMENT, LOCATION, TIME, and BENEFICIARY support abstraction across syntactic frames and lexical variation. This level of representation identifies *who did what to whom, where, and when* without committing to deeper logical structure ([Jurafsky and Martin, 2025](#)). Shallow semantics refers to the intermediate layer commonly modelled in semantic role labelling ([Jurafsky and Martin, 2025](#)).

A.3 Predicate–Argument Binding

Predicate–argument binding is the process of assigning thematic roles to the appropriate argument tokens. It forms the structured substrate on which more complex semantic composition builds: without correct role assignment, higher-level interpretation (e.g., quantification, scope, or discourse reference) cannot proceed. Our study isolates this binding mechanism, focusing on shallow semantics, and does not address deeper semantic phenomena such as quantifier scope or anaphora.

A.4 Computational Instantiation in Transformers

In transformer models, predicate–argument binding might arise through: (i) attention heads routing in-

formation between predicates and their arguments, (ii) distributed representations encoding role–filler associations, or (iii) localised circuits whose coordinated activity is *causally necessary* for role prediction. Our study tests for such circuits by combining causal edge-attribution patching, temporal emergence analysis, and cross-model comparison. Our goal is to determine whether transformers encode thematic roles via *computationally indispensable* mechanisms that are structurally localised, temporally trackable, and partially conserved across architectures.

Relevance for interpretability. If transformers encode predicate–argument binding via compact circuits, this suggests that meaningful semantic abstractions emerge naturally during training. Such findings provide mechanistic links between representation learning and the acquisition of linguistic structure, and offer principled targets for editing semantic behaviour.

B Dataset Generation Formalisation and Intervention Specifications

B.1 Task: Role-Cross Next-Token Prediction

We construct **role-cross minimal pairs** to isolate the semantic role processing. Each pair consists of two incomplete prompts that differ only in their role-indicating scaffold:

$$\begin{aligned} x^{(r)} &= \text{“The agent verb theme scaffold}^{(r)}\text{”}, \\ x^{(s)} &= \text{“The agent verb theme scaffold}^{(s)}\text{”}, \end{aligned} \quad (12)$$

where scaffold^(r) (e.g., “to the”, “about the”) indicates the semantic role r of the next token. The two contexts are constructed such that:

- In clean context $x^{(r)}$, target token $y^{(r)}$ is role-appropriate and most probable
- In corrupted context $x^{(s)}$, a **different** token $y^{(s)}$ appropriate for role s should be most probable
- Both $y^{(r)}$ and $y^{(s)}$ are drawn from a cross-role lexicon, ensuring they are valid fillers for their respective roles, but not for each other’s roles

Evaluation Task. The model performs role-cross prediction correctly if it predicts the role-appropriate target in each context:

$$\begin{aligned} \text{Accuracy} &= \mathbb{1}\llbracket y^{(r)} = \arg \max_v P_\theta(v \mid x^{(r)}) \rrbracket \\ &\quad \wedge \mathbb{1}\llbracket y^{(s)} = \arg \max_v P_\theta(v \mid x^{(s)}) \rrbracket \end{aligned} \quad (13)$$

This measures whether the model correctly binds different role fillers based solely on the role scaffold, holding agent, verb, and theme constant.

Example.

$$\begin{aligned} x^{(\text{GOAL})} &= \text{“The driver sent the wall to the”} \\ &\rightarrow y^{(\text{GOAL})} = \text{“office”} \\ x^{(\text{TOPIC})} &= \text{“The driver sent the wall about the”} \\ &\rightarrow y^{(\text{TOPIC})} = \text{“plan”} \end{aligned}$$

The scaffolds “to the” and “about the” have the same token length (parity), but should activate different role-specific vocabularies.

B.2 Frame-Based Template Construction

We construct role-cross pairs inspired by PropBank (Palmer et al., 2005) and FrameNet (Baker et al., 1998) annotations using frame-based templates. Each template consists of:

- **Frame:** Semantic structure (e.g., TRANSFER, COMMUNICATION)
- **Verb:** Single-token predicate (e.g., “sent”, “prepared”)
- **Scaffold:** Role-indicating preposition phrase (e.g., “to the” for GOAL, “about the” for TOPIC)
- **Agent:** Single-token subject (e.g., “driver”, “worker”)
- **Theme:** Single-token object (e.g., “wall”, “package”)
- **Target:** Role-specific single-token filler (e.g., “office” for GOAL, “plan” for TOPIC)

Single-Token Constraint. All lexical items must tokenise to exactly one token when preceded by a space (GPT-NeoX/Llama convention). We validate using the target model’s tokeniser and filter out multi-token words. This ensures: (i) precise position alignment for activation patching, and (ii) unambiguous attribution to specific lexical items.

Token Parity Enforcement. For each role-cross pair $(x^{(r)}, x^{(s)})$, we enforce **strict token-level parity**: $|\text{toks}(x^{(r)})| = |\text{toks}(x^{(s)})|$. This is achieved by:

1. Grouping scaffolds by token length (e.g., 2-token: “to the”, “in the”, “about the”; 1-token: “at”, “on”)

2. Only pairing roles whose scaffolds have matching token lengths
3. Keeping agent, verb, and theme constant across pairs
4. Rejecting pairs that violate parity after substitution

Token parity is **essential for EAP-IG**, as activation differences $\Delta_u = \mathbf{z}_u^{(r)} - \mathbf{z}_u^{(s)}$ require position-aligned representations.

Role-Specific Lexicons. Each semantic role has a curated lexicon of plausible fillers:

- **Goal:** Places and people (“office”, “student”, “school”)
- **Location:** Places (“kitchen”, “office”, “park”)
- **Instrument:** Tools (“hammer”, “knife”, “drill”)
- **Material:** Substances (“steel”, “wood”, “stone”)
- **Topic:** Abstract concepts (“plan”, “idea”, “issue”)
- **Beneficiary:** People (“student”, “client”, “friend”)

Lexicons are designed such that tokens are **role-discriminative**: strongly preferred in their primary role but less probable in other roles (e.g., “hammer” is a good INSTRUMENT but bad TOPIC).

B.3 Generation Procedure

For each target role r and desired sample size N :

1. Sample target token $y^{(r)}$ from role r ’s lexicon
2. Identify corrupt role $s \neq r$ such that:
 - Scaffolds for r and s have matching token lengths (parity constraint)
 - Role s has a distinct lexicon (ensures different target $y^{(s)}$)
3. Sample verb-agent-theme triple compatible with both roles
4. Construct clean prefix $x^{(r)}$ with scaffold^(r)
5. Construct corrupted prefix $x^{(s)}$ by replacing scaffold^(r) with scaffold^(s)
6. Sample foil token $y^{(s)}$ from role s ’s lexicon
7. Validate:
 - Token parity: $|\text{toks}(x^{(r)})| = |\text{toks}(x^{(s)})|$
 - No leakage: Neither $y^{(r)}$ nor $y^{(s)}$ appears in prefixes

- All tokens are single-token
- 8. If validation passes, add $(x^{(r)}, x^{(s)}, y^{(r)}, y^{(s)})$ to dataset
- 9. Repeat until N valid pairs obtained (patience limit: $30N$ attempts)

B.4 Filtering Procedure

We filter generated pairs to retain only examples where the model predicts the role-appropriate target in **both** contexts.

This ensures circuits are functionally active: the model successfully performs role-specific binding in both clean and corrupted contexts. Examples where either prediction is incorrect are discarded, as they would not reflect active role processing.

B.5 Dataset Statistics

After filtering with Pythia-1B, we obtain:

- **Total examples:** 4740 role-cross pairs across 8 roles
- **Token parity:** 100% (all pairs have matching token counts)
- **Dual prediction accuracy:** 100% (by construction, post-filtering: model predicts correct target in both clean and corrupted contexts)
- **Cross-role coverage:** Each role has at least ≥ 350 examples

Table 6 provides per-role breakdown.

C EAP-IG formalisation

EAP-IG combines the causal faithfulness of activation patching (Meng et al., 2022; Wang et al., 2022) with the path-sensitivity of integrated gradients (Sundararajan et al., 2017), addressing key limitations of alternative approaches. We detailed its steps below.

C.1 Transformers as Acyclic Graphs

We adopt the graph-theoretic representation from Hanna et al. (2024), modelling transformer computation as a directed acyclic graph $\mathcal{G} = (\mathcal{V}, \mathcal{E})$ at module \times position granularity. A node $u \in \mathcal{V}$ corresponds to a specific module output:

$$u \in \mathcal{V} \iff u = (\text{type}, \ell, h, i), \quad (14)$$

type $\in \{\text{AttnHead}, \text{MLP}\}$,

where ℓ is layer index, i is the token position in the sequence, and h is head index for attention

Table 6: Role-cross dataset statistics after filtering for all models. All examples satisfy: (i) strict token parity between clean and corrupted contexts, (ii) model predicts target correctly in both contexts.

Examples per Role	<i>Pythia-14M</i>	<i>Pythia-410M</i>	<i>Pythia-1B</i>	<i>LLaMA-1B</i>
Goal	845	895	1052	491
Location	904	673	975	815
Source	667	1206	505	612
Path	802	894	707	959
Instrument	459	1460	1212	1098
Beneficiary	773	837	621	1502
Topic	1120	1323	491	1179
Time	681	645	753	734

heads; $h = \emptyset$ for MLPs. The activation $\mathbf{z}_u \in \mathbb{R}^d$ is the contribution of that module to the residual stream at position i .

An edge $(u \rightarrow v) \in \mathcal{E}$ exists if \mathbf{z}_u is linearly mixed into the pre-activation input \mathbf{s}_v of node v via the residual stream and layer normalisation. This yields a fine-grained graph where each edge corresponds to a specific causal pathway between modules.

C.2 EAP-IG Scoring Procedure

For each clean/corrupt pair, let $\mathbf{x}^{(c)}$ and $\mathbf{x}^{(r)}$ be the input embedding sequences for $x^{(c)}_1 : t$ and $x^{(r)}_1 : t$, respectively, and $\mathbf{z}_u^{(c)}$ be the activation of node u under $x_{1:t}^{(c)}$, and $\mathbf{z}_u^{(r)}$ be activation of node u under $x_{1:t}^{(r)}$. We compute causal edge attributions through the following protocol:

- Cache activations:** Run the model on both versions to obtain $\mathbf{z}_u^{(c)}$ and $\mathbf{z}_u^{(r)}$ for all nodes u .
- Compute source deltas:** $\Delta_u = \mathbf{z}_u^{(r)} - \mathbf{z}_u^{(c)}$.
- Interpolate inputs:** Define the straight-line interpolation $\mathbf{x}(\alpha) = \mathbf{x}^{(r)} + \alpha(\mathbf{x}^{(c)} - \mathbf{x}^{(r)})$ for $\alpha \in [0, 1]$.
- Gradient sampling:** For m evenly spaced α_k and destination node v , at each step k , run a forward pass with input $\mathbf{x}(\alpha_k)$ and compute the gradient of the loss with respect to v 's pre-activation input: $\mathbf{g}_v^{(k)} = \partial L(\mathbf{x}(\alpha_k)) / \partial \mathbf{s}_v \in \mathbb{R}^d$.
- Integrate:** Average over m to obtain the integrated gradient estimate $\bar{\mathbf{g}}_v = \frac{1}{m} \sum_{k=1}^m \mathbf{g}_v^{(k)}$.
- Edge score:** $S_{u \rightarrow v}^{\text{IG}} = \Delta_u^\top \bar{\mathbf{g}}_v \in \mathbb{R}$.

Intuitively, $S_{u \rightarrow v}^{\text{IG}}$ approximates the first-order change in the loss if the contribution of u to v 's input were replaced by its corrupted counterpart, *averaged* along the naturalistic path from corrupt to clean inputs. By integrating over α , the estimate reduces sensitivity to local saturation at the clean point and captures non-linear response accumulated along the path.

C.3 Score Normalisation and Aggregation.

To enable fair comparison across layers and modules with different activation scales, we report both raw and normalised attribution scores. The normalised score for edge $(u \rightarrow v)$ is:

$$\tilde{S}_{u \rightarrow v}^{\text{IG}} = \frac{\Delta_u^\top \bar{\mathbf{g}}_v}{\|\Delta_u\|_2 \|\bar{\mathbf{g}}_v\|_2 + \varepsilon}, \quad \varepsilon = 10^{-8}. \quad (15)$$

Unless otherwise stated, aggregated statistics are computed on raw scores; normalization is used for scale-invariant concentration measures.

For role-specific analysis, we aggregate edge scores into role-layer heatmaps by summing absolute scores over edges sharing a destination module:

$$\text{Importance}^{(r)}(\text{layer} = \ell, \text{head} = h) = \sum_{\substack{(u \rightarrow v) \in \mathcal{E}: \\ v = (\text{AttnHead}, \ell, h, \cdot)}} |S_{u \rightarrow v}^{\text{IG}}|, \quad (16)$$

and analogously for MLPs.

C.4 Circuits Evaluation metrics

Faithfulness: the proportion of the clean–corrupt discrimination preserved by \mathcal{C} :

$$\text{Faithfulness}(\mathcal{C}) = \frac{M(\mathcal{C}) - M(\emptyset)}{M(\mathcal{E}) - M(\emptyset)}, \quad (17)$$

where $M(\mathcal{C})$ is the metric in Section 3.2 under \mathcal{C} , $M(\mathcal{E})$ under all edges patched, and $M(\emptyset)$ under none patched.

Temporal Consistency. Jaccard stability of top- K edge sets between checkpoints t and t' :

$$\text{Stability}(\mathcal{C}_t, \mathcal{C}_{t'}) = \frac{|\mathcal{C}_t \cap \mathcal{C}_{t'}|}{|\mathcal{C}_t \cup \mathcal{C}_{t'}|}. \quad (18)$$

High stability indicates that once a role circuit emerges, it persists across training.

Bootstrap CI for Change-point We estimate a split point t in $(x = \text{step}, y = \text{faithfulness})$ by minimising the summed residuals of two OLS lines on $\llbracket x_1, \dots, x_t \rrbracket$ and $\llbracket x_{t+1}, \dots, x_n \rrbracket$ with a minimum segment length of 3. For a 95% CI, we resample pairs (x, y) with replacement, sort by x , re-fit the split, map the bootstrap split x_t^* back to the original grid, and take the 2.5/97.5 percentiles over 1,000 replicates. We report the point estimate \hat{t}_c and the percentile CI over steps.

D Computation and parameters specifications

D.1 Hyperparameter Selection

All hyperparameters were selected based on circuit size constraints, computational feasibility, and robustness to measurement noise. We report choices for attribution, sparsity measurement, emergence detection, and cross-scale comparison.

Attribution (EAP-IG).

- **Integrated gradients steps:** 5. We use only 5 steps due to the large number of training checkpoints analysed. Ablation tests (not shown) confirmed 5 steps provide stable attributions whilst maintaining computational tractability for multi-checkpoint analysis.
- **Metric:** Negative log-probability of the role-appropriate target token in the clean context: $\mathcal{L} = -\log P_\theta(y^{(r)} \mid x^{(r)})$. This loss quantifies the model’s confidence in correct role binding.

Sparsity and Localization (RQ1).

- **Top-K node mass:** $K \in \{5, 10, 20\}$. We report the fraction of total attribution mass captured by the top- K highest-mass nodes. These values span from highly concentrated cores ($K=5$) to broader component sets ($K=20$).
- **Gini coefficient:** Computed over all in-circuit node masses (nodes with non-zero attribution). Higher Gini indicates more unequal mass distribution (tighter concentration).

- **Rationale:** All discovered circuits contain fewer than 40 active nodes at convergence, making $K=20$ a natural threshold capturing approximately 50% of the component space whilst focusing on high-importance nodes.

Emergence Dynamics (RQ2).

- **Indispensability threshold:** $M(\mathcal{C}_t) - M(\mathcal{E}_t) < 0$ for ≥ 2 consecutive checkpoints. Circuit performance must fall persistently below baseline to avoid transient noise.
- **Change-point detection:** Two-segment piecewise linear regression applied to faithfulness and Top-20 mass trajectories. Bootstrap resampling ($n=1,000$) estimates 95% confidence intervals. Minimum segment length: 2 checkpoints (prevents overfitting to single-step noise).
- **Consolidation criterion:** Jaccard overlap ≥ 0.6 between top- $K=20$ node sets over a 2-step sliding window. This threshold balances sensitivity (detects stabilisation) against noise (ignores minor fluctuations).

Cross-Scale Comparison (RQ3).

- **Node/edge overlap:** Top- $K=30$ components by absolute attribution mass. We increase K from 20 (used in RQ1/RQ2) to 30 for cross-scale comparison because larger models (410M, 1B) have more active nodes; $K=30$ ensures we compare substantive component sets whilst maintaining focus on high-importance nodes.
- **Spectral distance:** Computed on top- $K=50$ edges using the lowest $k=20$ Laplacian eigenvalues. We use more edges ($K=50$) for spectral analysis than overlap ($K=30$) because eigenvalue computation requires sufficient connectivity to yield stable spectra. The first 20 eigenvalues capture low-frequency flow structure whilst remaining computationally tractable.
- **Rationale:** Since all circuits contain <40 active nodes at convergence, $K=30$ captures $\sim 75\%$ of the component space. This "hard 50% rule" ensures overlap metrics reflect substantive similarity rather than trivial peripheral agreement. For edges, $K=50$ balances spectral stability with focus on high-attribution connections.

Data Filtering.

- **Correctness criterion:** Retain only examples where the model predicts the role-appropriate

target correctly in **both** clean and corrupted contexts at baseline (full model). Formally: $y^{(r)} = \arg \max_v P_\theta(v \mid x^{(r)})$ AND $y^{(s)} = \arg \max_v P_\theta(v \mid x^{(s)})$.

- **Rationale:** This dual-correctness filter ensures discovered circuits are functionally active—the model successfully performs role binding in both contexts, guaranteeing circuits supporting this capability are present and engaged. Analysing only correctly predicted examples is standard practice in mechanistic interpretability (Wang et al., 2022; Conmy et al., 2023) as it isolates functional mechanisms rather than failure modes.

Computational Constraints. All experiments were conducted on an NVIDIA RTX A6000 GPU. Attribution over multiple checkpoints required approximately 5 min per role for *Pythia-1b*. The choice of 5 IG steps was necessary to complete the temporal analysis within feasible compute budgets whilst maintaining attribution stability, as confirmed by spot-checks with higher step counts on selected checkpoints.

Software Specification. Experiments were conducted using Python 3.11.13 with NumPy 1.26.4, scikit-learn 1.7.0, scipy 1.15.3, seaborn 0.13.2, tokenizers 0.21.1, torch 2.7.1, transformer-lens 2.16.1, and transformers 4.52.4, and trace 0.2.0.

E Metric Definitions and Interpretation

Setup. All metrics are computed on the *in-circuit* subgraph for each *role* and *training step*. Let $G = (V, E)$ be a directed graph whose vertices $v \in V$ are components (attention heads al.h , MLPs $m\ell$, special nodes input/logits), and whose edges $e = (u \rightarrow v) \in E$ carry an attribution score $s(e) \in \mathbb{R}$ and a type $\tau(e) \in \{\text{Q}, \text{K}, \text{V}, \text{Flow}\}$. Unless stated, strength uses absolute attribution $|s(e)|$.

Node mass. Incident absolute attribution:

$$\begin{aligned} \text{mass}(v) &= \sum_{e \in \text{Inc}(v)} |s(e)|, \\ \text{Mass}(G) &= \sum_{v \in V} \text{mass}(v). \end{aligned} \quad (19)$$

Note: $\text{Mass}(G) = 2 \sum_{e \in E} |s(e)|$ since each edge contributes to two endpoints. We also report **Total mass** as a proxy for role salience at a step.

Sparsity & Targeting (per role × step)

Top- K node-mass proportion.

$$\text{TopK}(K) = \frac{\sum_{i=1}^K m_{(i)}}{\sum_{i=1}^{|V|} m_{(i)}}, \quad (20)$$

$$m_{(1)} \geq \dots \geq m_{(|V|)}.$$

Range $\llbracket 0, 1 \rrbracket$; higher \Rightarrow stronger sparsity. We report $K \in \{5, 10, 20\}$.

Top- P coverage. Minimal K such that $\text{TopK}(K) \geq P$, for $P \in \{0.80, 0.90, 0.95\}$. Lower K indicates higher sparsity.

Gini coefficient (node mass). Standard Gini on nonnegative masses; range $\llbracket 0, 1 \rrbracket$ (1 = all mass on one node). Primary comparator for **sparse localisation** (RQ1).

comparable across graphs of different sizes.

Structural / Connectivity (per role × step)

Nodes, Edges. $|V|$ and $|E|$ of the in-circuit graph.

Density. We use NetworkX’s directed density:

$$\text{density}(G) = \frac{|E|}{|V|(|V| - 1)} \in \llbracket 0, 1 \rrbracket, \quad (21)$$

assuming no self-loops. (*Implementation:* nx.density.)

Reciprocity. Fraction of directed edges participating in reciprocated pairs:

$$\text{recip}(G) = \frac{L_{\leftrightarrow}}{L}. \quad (22)$$

Average out-degree / weighted out-degree.

$$\begin{aligned} \overline{\text{deg}^+} &= \frac{1}{|V|} \sum_v \text{deg}^+(v), \\ \overline{\text{deg}_w^+} &= \frac{1}{|V|} \sum_v \sum_{(v \rightarrow u) \in E} |s(v \rightarrow u)|. \end{aligned} \quad (23)$$

Edge-type fractions.

$$\begin{aligned} \text{frac}_T &= \frac{|\{e \in E : \tau(e) = T\}|}{|E|}, \\ T &\in \{\text{Q}, \text{K}, \text{V}, \text{Flow}\}, \\ \sum_T \text{frac}_T &= 1. \end{aligned} \quad (24)$$

Metric	Range	High	Low
Top- K mass	$[0, 1]$	concentrated circuit (RQ1)	diffuse attribution
Top- P coverage (K)	\mathbb{N}	few nodes capture P (sparse)	many nodes needed
Gini (mass)	$[0, 1]$	strong sparsity (RQ1)	uniform mass
Density	$[0, 1]$	saturated links (post- \hat{t}_c)	sparse links
Reciprocity	$[0, 1]$	feedback motifs	feed-forward routing
Avg out-degree	$\mathbb{R}_{\geq 0}$	broad fan-out	narrow fan-out
Avg weighted out-degree	$\mathbb{R}_{\geq 0}$	strong influence spread	weak influence
Edge-type mix	simplex	routing vs. residual balance	—
Bridges	\mathbb{N}	bottlenecks (ablation targets)	redundancy
Layer span	\mathbb{N}	deeper integration	shallow circuit
Avg betweenness	$[0, 1]$ (norm.)	coordinator hubs	flat routing
Top- K Jaccard (step)	$[0, 1]$	persistent circuit	unstable set
Cross-model Jaccard	$[0, 1]$	architectural consistency	family/scale drift
Spectral distance d_{spec}	$\mathbb{R}_{\geq 0}$	similar flow geometry	divergent geometry

Table 7: Interpretation guide for graph metrics.

Bridges (undirected projection). Count edges whose removal disconnects the *undirected* projection of G (structural bottlenecks).

Layer span.

$$\text{layer_span} = \max_{v \in V} \text{layer}(v) - \min_{v \in V} \text{layer}(v). \quad (25)$$

Average betweenness centrality. $\overline{C_B} = \frac{1}{|V|} \sum_v C_B(v)$ on the directed graph (normalized; may use sampling for efficiency).

Emergence & Stability (per role)

Detectability t_{det} (optional). First step where faithfulness exceeds an early-phase baseline plus 2σ (baseline/variance from the first 2 checkpoints), persisting for ≥ 2 checkpoints.

Indispensability t_{ind} . Earliest step where ablating the discovered circuit yields a statistically significant performance drop that *persists* for at least 2 subsequent checkpoints.

Change-point \hat{t}_c (with bootstrap CI).

Two-segment least-squares on $y_t \in \{\text{faithfulness}, \text{TopK}(K)\}$ with a minimum segment length of 3. We report \hat{t}_c with a nonparametric bootstrap 95% CI.

Consolidation t_{cons} . Earliest step post- \hat{t}_c where Top- K node sets stabilise: $\text{Jaccard}(V_t^{(K)}, V_{t'}^{(K)}) \geq 0.6$ for a 3-step window (persistence = 2), with $K=20$.

Cross-scale / Cross-role Similarity

Node/edge overlap across models. Mean Jaccard of Top- K node/edge sets between two models, averaged over common checkpoints. (Defaults: $K=30$.)

Spectral similarity. For symmetrised, weighted Laplacians ($w_{uv} = |s(u \leftrightarrow v)|$),

$$d_{\text{spec}}(G_i, G_j) = \text{RMSE}(\lambda_{1:k}(G_i), \lambda_{1:k}(G_j)),$$

where $\lambda_{1:k}$ are the k smallest eigenvalues. Lower is more similar. (Defaults: build undirected graphs from the Top-50 edges by $|s|$, $k=20$.)

Within-model role overlap. Jaccard of Top- K nodes between roles at fixed steps (specialisation vs. shared scaffolding).

Computation Conventions

- Mass/strength metrics use absolute attributions $|s(e)|$; sign-sensitive analyses are reported separately.
- Type fractions follow RDF edge labels $\tau(e) \in \{\text{Q, K, V, Flow}\}$.
- Density uses `nx.density` on directed graphs (no self-loops). Bridges are computed on the undirected projection.

Causal Flow Visualisation The causal flow diagrams (e.g., Figure 2) visualise the dominant information pathways within discovered circuits. We construct a directed graph $G = (V, E)$ where nodes V represent model components (e.g., attention heads $a_{\ell,h}$, MLP layers m_ℓ , and output logits) and edges E represent causal attribution

paths with weights w_{uv} quantifying the contribution of component u to component v . **Edge selection.** Rather than visualising the complete circuit graph, we filter to the top- k edges by attribution magnitude $|w_{uv}|$ among those marked as in-circuit. This selective visualisation serves two purposes: (1) it highlights the *dominant* computational pathways that account for the majority of causal effect, as circuits exhibit high concentration, and (2) it ensures interpretability, as dense graphs obscure rather than illuminate mechanistic structure. We use quantile-based thresholds (95th percentile by default) with a minimum edge count (12) to ensure sufficient context for interpretation. **Graph layout.** Nodes are positioned via multipartite layout by layer depth ℓ , flowing left-to-right from inputs ($\ell = -1$) through transformer layers to logits ($\ell = L + 1$). Edge attributes encode: width $\propto |w_{uv}|$ (attribution strength), colour by edge type (Query/Key/Value composition versus residual flow), and style (solid for positive attribution, dashed for negative suppression). This representation exposes: (i) critical computational pathways for each semantic role, (ii) layer-wise concentration of circuit activity, and (iii) coordination patterns between attention mechanisms versus direct residual connections.

Interpretation Cheat Sheet

See Table 7, with full method algorithm in 1.

Default parameters used in the paper. Unless otherwise noted: consolidation uses $K=20$, Jaccard ≥ 0.6 , persistence = 2; cross-model overlap uses $K=30$; spectral similarity uses Top-50 edges and $k=20$ eigenvalues.

F Full Results

We add the full results for *Pythia-14m*, *Pythia-410M* and *LLaMA-1B*.

F.1 RQ1: Full Localisation Results

This section provides the full localisation analyses for all semantic roles, model scales, and training checkpoints, complementing the representative results in the main text. For each role, we report (i) mass-concentration statistics, (ii) sparsity and coverage metrics, and (iii) stability of component sets over checkpoints.

Mass concentration and sparsity. Table 8 reports the Top- K mass ($K \in \{5, 10, 20\}$) for all roles and models at the final checkpoint (143k

Algorithm 1 COMPASS: Causal-Temporal Circuit Discovery

Require: Model checkpoints $\{\theta_t\}_{t=0}^T$, role-cross dataset D , role $r \in \mathcal{R}$, top- K threshold
Ensure: Circuit $\mathcal{C}_t^{(r)}$ for each t ; emergence times $(t_{\text{ind}}, \hat{t}_c, t_{\text{cons}})$

- 1: **Phase 1: Causal Localisation (EAP-IG)**
- 2: **for** each checkpoint $t = 0, \dots, T$ **do**
- 3: Compute CNP scores $\{\Delta_{\theta_t}(y; r, s)\}$ for all $(x^{(r)}, x^{(s)}) \in D$
- 4: Run EAP-IG to obtain edge attributions $\{S_{u \rightarrow v}^{\text{IG}}\}_{e \in \mathcal{E}}$ (Appendix C)
- 5: Normalise: $\tilde{S}_{u \rightarrow v}^{\text{IG}} \leftarrow S_{u \rightarrow v}^{\text{IG}} / \sum_e |S_e^{\text{IG}}|$
- 6: Extract circuit: $\mathcal{C}_t^{(r)} \leftarrow \text{TopK}(\{|\tilde{S}_{u \rightarrow v}^{\text{IG}}|\}, K)$
- 7: **end for**
- 8: **Phase 2: Temporal Monitoring**
- 9: **for** each checkpoint $t = 0, \dots, T$ **do**
- 10: Compute faithfulness F_t via ablation (Eq. 6)
- 11: Compute stability S_t via Jaccard (Eq. 7)
- 12: Compute structural metrics: Top- K node mass, Gini coefficient
- 13: **end for**
- 14: **Phase 3: Emergence Detection**
- 15: Detect indispensability: $t_{\text{ind}} \leftarrow \min\{t : M_t(\mathcal{E}) - M_t(\mathcal{C}_t) > \epsilon \text{ for } \geq 2 \text{ steps}\}$
- 16: Estimate functional transition: $\hat{t}_c \leftarrow \arg \max_t R^2(\text{PiecewiseLinear}(\{F_t\}))$ with bootstrap CIs
- 17: Detect consolidation: $t_{\text{cons}} \leftarrow \min\{t : S_t \geq 0.6 \text{ for } \geq 2 \text{ steps}\}$
- 18: **return** $\{\mathcal{C}_t^{(r)}\}_{t=0}^T, (t_{\text{ind}}, \hat{t}_c, t_{\text{cons}})$

steps). Across all settings, Top-20 nodes capture between 83% and 99% of attribution mass, confirming that role circuits remain highly concentrated even in larger scales.

Coverage: minimal node set sizes. Table 9 reports the smallest k achieving 80%, 90%, and 95% mass. Across all roles and models, fewer than 30 nodes suffice for 95% coverage, again confirming that circuits remain compact even in 1B-scale architectures.

Cross-scale similarity of component sets. Figures 6 and 7 summarise how role circuits align across PYTHIA-14M, PYTHIA-410M, and PYTHIA-1B. Node-level Top-30 overlaps vary by role, ranging from $J_V \approx 0.24$ –0.31 between 14M

Role	PYTHIA-14M			PYTHIA-410M			LLAMA-1B		
	T-5	T-10	T-20	T-5	T-10	T-20	T-5	T-10	T-20
BENEFICIARY	0.465	0.769	0.988	0.345	0.58	0.906	0.4	0.657	0.939
INSTRUMENT	0.445	0.596	0.833	0.445	0.596	0.833	0.484	0.697	0.895
LOCATION	0.368	0.557	0.841	0.368	0.557	0.841	0.413	0.636	0.882
TIME	0.397	0.628	0.974	0.397	0.628	0.974	0.443	0.677	0.961

Table 8: Top- K mass concentration at final checkpoint (143k steps). Values show fraction of total attribution mass captured by K highest-mass nodes.

Role	PYTHIA-14M	PYTHIA-410M	LLAMA-1B
BENEFICIARY	11 / 13 / 15	16 / 20 / 23	14 / 17 / 22
INSTRUMENT	11 / 14 / 17	19 / 24 / 28	15 / 21 / 25
LOCATION	12 / 15 / 17	19 / 23 / 27	17 / 21 / 25
TIME	10 / 13 / 17	15 / 18 / 20	14 / 17 / 20

Table 9: Minimal node count k required to capture 80% / 90% / 95% of total attribution mass at final checkpoint (143k steps).

and 1B to $J_V \approx 0.37\text{--}0.56$ between 410M and 1B. TIME shows the strongest cross-scale alignment (up to $J_V=0.56$ for 410M \leftrightarrow 1B), indicating that its circuits are both highly compact and structurally similar at larger scales. Edge-level overlaps are consistently lower ($J_E \approx 0.06\text{--}0.18$), confirming that connection patterns diverge more than the identity of high-importance nodes. Spectral distances are smallest for the 410M \leftrightarrow 1B pairs ($d_{\text{spec}} \approx 0.006\text{--}0.018$) and larger when 14M is involved ($d_{\text{spec}} \approx 0.05\text{--}0.15$), suggesting that while small models already recruit broadly similar components, the overall information-flow geometry only stabilises once scale increases.

Summary. Across all roles and model scales, we find that semantic-role circuits localise to highly compact subgraphs whose attributional mass is dominated by a small, stable subset of nodes. Final-step Top-20 mass consistently exceeds 0.83 (and reaches 0.97–0.99 for several roles; Table 8), and only $\sim 15\text{--}28$ nodes are required to capture 95% of total mass (Table 9). These component sets remain stable across training checkpoints, with only minor turnover in the highest-mass nodes. Structural metrics further reveal a characteristic pattern of refinement: active node sets contract slightly over training while density increases, indicating consolidation around a pruned but increasingly interconnected core. Together, these results show that role circuits are both *spatially localised* and *structurally coherent*, forming compact causal pathways that become progressively more organised as training proceeds.

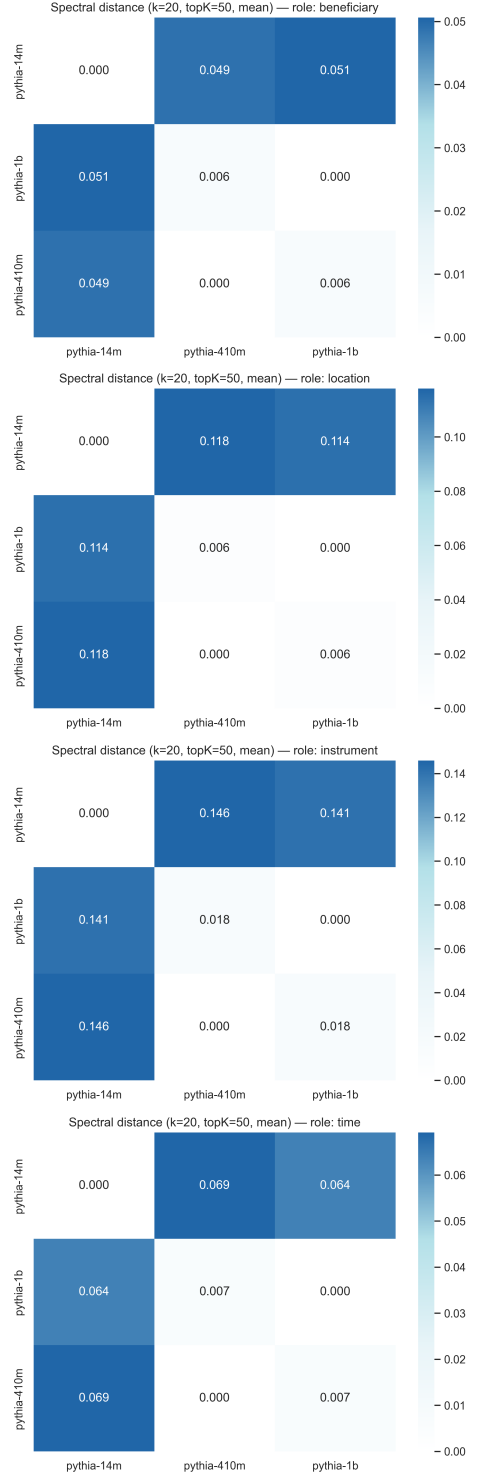


Figure 6: Cross scale spectral distance

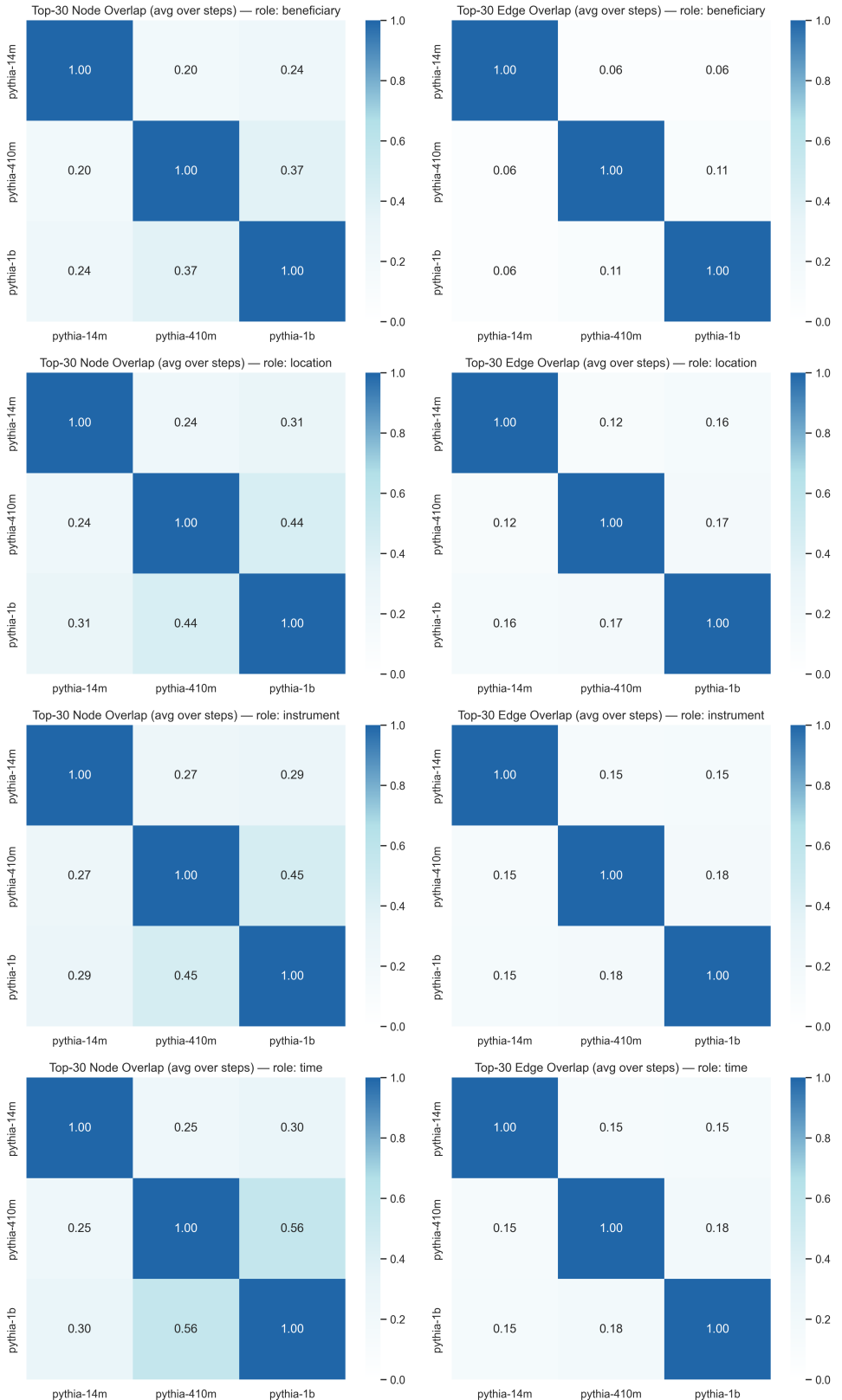


Figure 7: Cross scale spectral distance

F.2 RQ2: Full Emergence Dynamics

This appendix complements the main-text analysis by providing the full emergence dynamics results for PYTHIA–14M. We analyse three signals across training: faithfulness, indispensability, and structural consolidation, and compare them to change-point estimates derived from piecewise linear fits.

Indispensability. All roles eventually become causally necessary, but the timings vary by more than four orders of magnitude. INSTRUMENT circuits are useful from the first checkpoint ($t_{\text{ind}}=0$), LOCATION becomes indispensable early (1k steps), and GOAL follows at 5k. TIME emerges only at mid-training (71k steps), reflecting exceptionally delayed functional reliance. These heterogeneous timings indicate that roles differ substantially in both cue learnability and the optimisation pressure required for the model to commit to a stable causal pathway.

Faithfulness trajectories. Faithfulness curves exhibit pronounced non-monotonicity, with early rises, sharp drops, and late partial recoveries. INSTRUMENT peaks early and declines; TIME rises initially, crashes after 5–10k steps, and partially recovers; GOAL and LOCATION show smoother but still multi-phase dynamics. Importantly, these fluctuations do not correspond to abrupt structural changes: functional utility is unstable even when the underlying structure is already highly concentrated.

Structural consolidation. In contrast to faithfulness, structural metrics evolve smoothly. Top- K node sets stabilise extremely early for most roles (512 steps for GOAL, LOCATION, and TIME; 2k for INSTRUMENT). Thus, the model identifies the relevant components long before those components become functionally indispensable. Structural consolidation is therefore not the bottleneck in circuit emergence.

Change-point analysis. Two-segment piecewise fits to Top- K mass trajectories yield very wide bootstrap confidence intervals (e.g. TIME: [512, 10k]; INSTRUMENT: [64, 8k]), confirming that structural sparsification is gradual rather than concentrated at a discrete transition. Visual inspection of sparsity curves reveals smooth monotonic growth without identifiable inflection points. The structural substrate evolves continuously even when functional utility displays sharp changes.

Final-step sparsity. By convergence (143k steps), all circuits are highly compact: Top-20 mass ranges from 0.83–0.97, and only 20–28 nodes suffice to cover 95% of attribution. TIME is the most concentrated (95% mass in 20 nodes), whereas INSTRUMENT and LOCATION have slightly broader but still compact top-tiers.

Summary. Across all roles in PYTHIA–14M, emergence is a gradual process in which *structural* properties stabilise early and monotonically, while *functional* utility develops in a noisy, role-dependent manner. Indispensability can lag far behind consolidation (e.g. 70k-step lag for TIME), indicating that circuits may be structurally “pre-allocated” long before the model consistently relies on them. Together, these results support the conclusion that semantic-role circuits do not undergo discrete phase transitions but instead emerge through continuous refinement shaped by heterogeneous task signals and optimisation dynamics.

F.3 Additional Semantic Roles

In addition to the four core roles analysed in the main paper, we applied the COMPASS pipeline to four further predicate–argument relations frequently used in semantic role labelling, including PATH, SOURCE, and TOPIC. Figure 9 reports their emergence trajectories (faithfulness, density, Top- K mass) across training checkpoints.

Overall, these supplementary roles exhibit the same qualitative patterns identified for the main roles. Structural metrics (density and Top- K mass) increase smoothly and monotonically, consistent with gradual sparsification rather than discrete phase transitions. In contrast, faithfulness trajectories are highly variable: PATH shows an extremely sharp early increase, becoming highly faithful almost immediately, followed by stable mid-training behaviour. SOURCE rises early but then gradually declines, mirroring the non-monotonic pattern seen in TIME. TOPIC increases sharply at early steps before collapsing and then partially recovering, indicating heavy competition with other predictive cues. The extended GOAL set displays declining faithfulness after an early peak, despite stable and increasing structural sparsity. These patterns match the dissociation seen in the primary roles: *structural sparsity is stable and monotonic, but functional utility is noisy and task-pressure dependent*. As before, structure often stabilises long before a role becomes functionally useful.

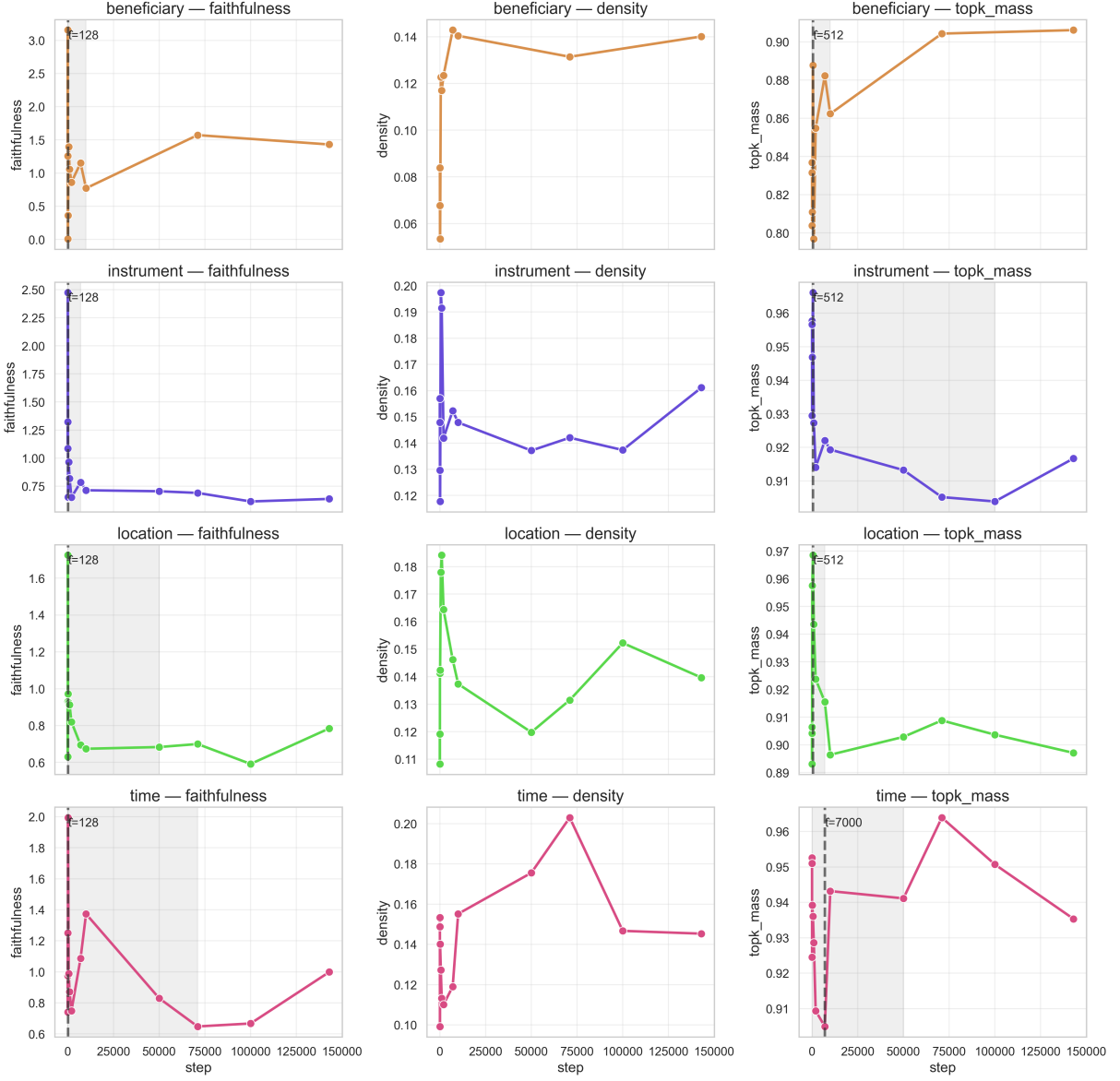


Figure 8: Emergence trajectories for each role in PYTHIA-1B. Left: faithfulness; middle: edge density; right: Top- K node mass (Top-20). Structural measures change smoothly over training, while faithfulness exhibits role-specific non-monotonicity.

Role	t_{ind} (steps)	t_{cons} (steps)	det. threshold
GOAL	0	1,000	1.021
PATH	—	8	0.803
SOURCE	0	8	1.215
TOPIC	512	1,000	1.168

Table 10: Indispensability (t_{ind}), and consolidation (t_{cons}) per role for 1B model.

Role	\hat{t}_c (steps)	95% CI
GOAL	128	[128, 7,000]
PATH	1,000	[8, 10,000]
SOURCE	1,000	[8, 10,000]
TOPIC	1,000	[8, 10,000]

Table 11: Change-point estimates for *Top- K node mass* via two-segment piecewise linear regression.

F.4 Circuit heterogeneity

While our results demonstrate that semantic role circuits consistently localise to compact subgraphs, the *internal organisation* of these circuits varies systematically across roles and training stages.

This variation reflects both the diversity of semantic cues associated with different roles and the flexibility of the model’s computational pathways. To characterise these differences, we examine the fine-grained structure of each circuit, its dominant

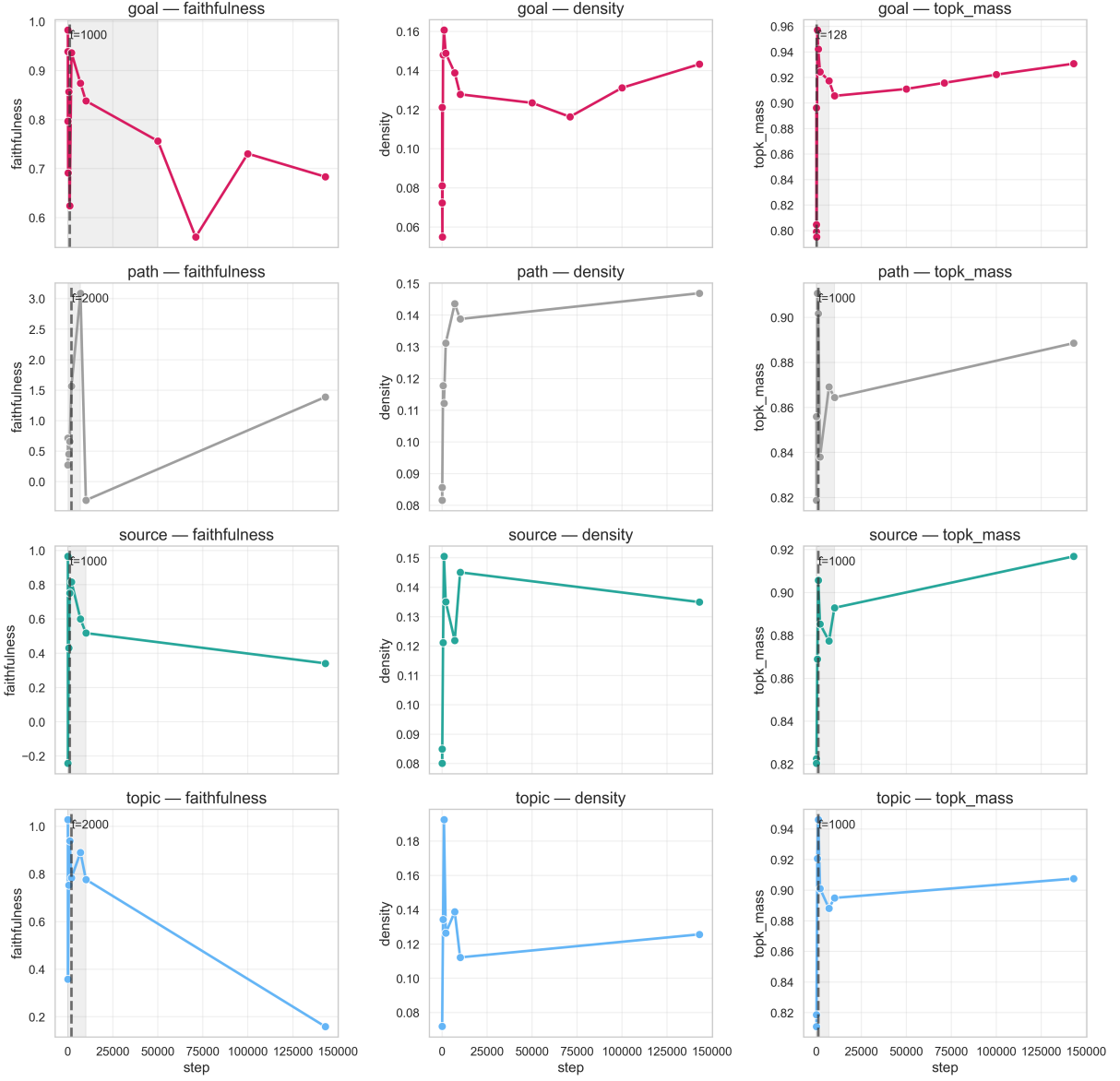


Figure 9: **Emergence trajectories for supplementary semantic roles for the 1B model.** Each row corresponds to a role; columns show faithfulness, density, and Top- K mass across training.

components, routing patterns, and evolution over training, using causal-flow visualisations derived from the top- $K=30$ nodes, with edges ranked by attribution magnitude at the 95th percentile threshold. These analyses reveal systematic and role-dependent heterogeneity in circuit structure, both at convergence and throughout developmental trajectories.

F.4.1 Architectural Stratification at Convergence

We identify four recurrent circuit architectural types at convergence (step 143k), distinguished by attention-head addition, integration depth, and reliance on value composition operations. Table 12

summarises the final circuit types, reporting node counts, attention head involvement, and dominant computational pathways.

Type 1: Lexical pattern matching. TIME and PATH rely predominantly on MLP computation with minimal or zero attention. TIME achieves the most extreme compression (16 nodes, zero attention), implementing a pure feed-forward pathway. PATH exhibits minimal attention involvement (18 nodes, 2 heads), we hypothesise a0.h6 provides early syntactic composition, while a12.h2 performs targeted value composition for the final pre-logit refinement. The dominant causal flow remains through the MLP backbone, with attention

Table 12: **Circuit categorisation across semantic roles at convergence.** Circuits stratify into four architectural types reflecting the computational demands of each role. Node counts reflect circuits extracted at the 95th percentile threshold with top- $K=30$ edges. “+V” indicates value composition edges; heads are listed in order of prominence in the causal-flow diagrams.

Type	Role	Nodes	Heads	Architecture
1	Time	16	0	Pure MLP chain; completely attention-free
	Path	18	2	Predominantly MLP with early framing (a0.h6) and late value composition (a12.h2+V)
2	Goal	18	3	Mid-layer extraction (a6.h0) with late integration (a12.h2+V, a14.h5)
	Topic	19	4	Early frame detection (a0.h2), mid-layer (a6.h0), late integration (a12.h2, a14.h5+V)
	Source	19	5	Rich multi-stage: early (a3.h7), mid (a6.h0), late (a12.h2, a14.h5, a15.h5)
3	Instrument	20	4	Mid-to-late extraction and integration (a3.h7, a6.h0, a12.h2, a14.h5)
	Location	20	4	Distributed integration (a1.h0, a12.h2, a13.h4, a14.h5)
4	Beneficiary	22	6	Complex late-stage architecture (a1.h0, a6.h0, a12.h2, a14.h5+V, a15.h0, a15.h5)

providing what seems to be an auxiliary support. Both roles mark a highly regular, closed set of expressions (e.g., temporal markers, path markers), enabling direct lexical classification without extensive need for contextual integration.

Type 2: Multi-stage compositional integration. GOAL, TOPIC, and SOURCE converge to moderate-complexity architectures (18–19 nodes, 3–5 attention heads) characterised by systematic multi-stage processing, with m0 being connected to the majority of other nodes in the circuit. GOAL (18 nodes, 3 heads) implements a clean two-stage architecture: mid-layer feature extraction at a6.h0, followed by late-stage integration at a12.h2+V (with value composition edge) and final refinement at a14.h5. The circuit exhibits sparse connectivity with clear information bottlenecks at m6 and m12. TOPIC (19 nodes, 4 heads) adds early integration of a0.h2, suggesting initial scaffold detection, then follows mid-to-late integration (a6.h0→a12.h2→a14.h5+V). Notably, value composition shifts to the final integration head (a14.h5+V) rather than at a12.h2, indicating part of feature extraction occurs at the pre-logit stage.

SOURCE (19 nodes, 5 heads) exhibits the richest attention architecture in this group: a3.h7, assumably for early instrumental/causal cue detection, a6.h0 for mid-layer feature gathering, and three late-stage heads (a12.h2, a14.h5, a15.h5) for final disambiguation. The circuit displays clear information flow through mid-layer MLPs (m3, m6) converging to late-stage integration at m12 and m15, with a15.h5 providing a final refinement pathway.

Type 3: Balanced hybrid architectures. INSTRUMENT and LOCATION exhibit moderate complexity (20 nodes, 4 heads each) with balanced MLP-attention integration. INSTRUMENT follows a hierarchical pattern: a3.h7 for early cue detection (likely detecting instrumental markers), a6.h0 for mid-layer extraction, and late-stage integration at a12.h2 and a14.h5. The circuit exhibits a clear bottleneck at m6, with multiple pathways converging to m12 and m14. Notably, INSTRUMENT lacks value composition at convergence, relying instead on positional routing through residual connections. LOCATION shows a more distributed architecture with attention heads spread across early (a1.h0), mid-late (a12.h2, a13.h4), and final (a14.h5) layers. The circuit maintains sparse MLP connectivity (m1, m13, m14) with attention providing targeted integration at multiple depths. Like INSTRUMENT, LOCATION lacks value composition edges, suggesting both roles have do not rely as much as others on active feature extraction mechanisms in favour of simpler, more efficient routing strategies by convergence.

Type 4: Complex late-stage integration with distributed refinement. BENEFICIARY has the most elaborate architecture at convergence (22 nodes, 6 heads), maintaining rich late-stage connectivity with dual final-layer heads. The circuit recruits a1.h0 for early processing, a6.h0 for mid-layer extraction, and four late-stage heads: a12.h2 for primary integration, a14.h5+V for feature extraction, and two heads (a15.h0, a15.h5) for final disambiguation. This architecture suggests BENEFICIARY requires parallel processing pathways to resolve persistent ambiguities, and probably the model maintains alternative hypotheses until the last computation step. The circuit’s relative complexity (22 nodes vs. 16–20 for other roles) and late-stage density indicate that beneficiary marking, despite being syntactically constrained (e.g., “for . . .”), requires more elaborate compositional reasoning than other participant roles, likely to dis-

tinguish benefactive readings from alternative interpretations.

F.4.2 Developmental Trajectories Across Training

Circuit evolution from initialisation (step 32) to convergence (step 143k) reveals role-specific developmental patterns. Figures 10, 11 and 12 present a sample of causal-flow diagrams at three key checkpoints, early training (step 32), mid-training (step 71000), and convergence (step 143000). These snapshots expose systematic differences in how semantic-role circuits emerge and stabilise. We study them for all roles below.

Universal early complexity followed by selective pruning. All roles begin training with diffuse connectivity and elevated node counts (15–23 nodes at step 32), reflecting initial hypothesis exploration. At initialisation, most circuits exhibit dense early-layer attention recruitment (multiple $a0.h^*$ heads) and extensive value composition edges, suggesting the model initially explores compositional integration strategies broadly across all roles. By mid-training (step 71000), circuits have begun to differentiate sharply: TIME achieves near-complete attention elimination (16 nodes, pure MLP), while BENEFICIARY maintains a rich multi-head architecture (21 nodes, 7 heads). At convergence (step 143000), final node counts (16–22) represent reductions from initialisation, with architectural consolidation complete and further refinement involving only edge-weight adjustments rather than topological restructuring.

Stratified consolidation and shared infrastructure. Roles follow distinct consolidation trajectories aligned with semantic complexity. What we assume are more **Template-matching roles** (TIME, PATH) eliminate most attention: TIME achieves pure MLP architecture by mid-training; PATH retains minimal heads ($a0.h6$, $a12.h2+V$).

Integration-dependent roles (GOAL, INSTRUMENT, LOCATION) stabilise core architectures by mid-training with only minor late refinement, converging to 2–4 attention heads with mid-to-late integration. **Multi-phase processing roles** (TOPIC, SOURCE, BENEFICIARY) undergo non-monotonic reorganisation: TOPIC contracts then reinstates early framing ($a0.h2$) and late value composition ($a14.h5+V$); SOURCE adds $a3.h7$ only at convergence; BENEFICIARY maintains persistent complexity with six heads including unique dual layer-

15 architecture ($a15.h0$, $a15.h5$) for parallel disambiguation.

Across trajectories, shared integration hubs emerge at predictable stages: $a12.h2$ (7/8 roles) stabilises by mid-training as universal late-stage integrator; $a14.h5$ (7/8 roles) emerges slightly later for pre-logit refinement; $a6.h0$ (5/8 roles) provides mid-layer extraction for compositional/discourse roles. Early-layer attention ($a0.h^*$, $a1.h^*$) is systematically pruned except in PATH, TOPIC, LOCATION, and BENEFICIARY, where explicit frame detection remains necessary. Value composition follows more of explore/prune/retain dynamics: broad at initialisation (6/8 roles), divergent at mid-training (4 roles eliminate, 1 intensifies to 3 V-ops), and selective at convergence (4 roles: PATH, GOAL, TOPIC, BENEFICIARY). V-edges shift spatially from early layers ($a0.h^*$, $a3.h^*$) to late integration heads ($a12.h2$, $a14.h5$), indicating feature extraction is preserved only where disambiguation proves irreducible.

F.5 Paraphrase-Based Within-Role Scaffold Controls (Pythia-1B)

To test whether role circuits encode *abstract semantic roles* rather than overfitting to a particular lexicalised scaffold, we construct a small within-role paraphrase control set for two representative roles: LOCATION and INSTRUMENT, and we study them over our reference model PYTHIA-1B.

Paraphrase construction. For each filtered example $(x^{(r)}, y^{(r)})$ in the role-cross dataset (Appendix B), we construct a within-role paraphrase by replacing the original scaffold with an alternative:

$$x_{\text{para}}^{(r)} = \text{"The agent verb theme scaffold}^{(r')}\text{"} \quad (26)$$

by replacing $\text{scaffold}^{(r)}$ with an alternative scaffold $\text{scaffold}^{(r')} \in \mathcal{S}^{(r)}$ such that:

- $\text{scaffold}^{(r')} \neq \text{scaffold}^{(r)}$
- $|\text{toks}(\text{scaffold}^{(r')})| = |\text{toks}(\text{scaffold}^{(r)})|$ (parity constraint)
- agent, verb, theme, and target head $y^{(r)}$ are unchanged

For example,

$$\begin{aligned} \mathcal{S}^{(\text{LOCATION})} &= \{\text{"in the"}, \text{"at the"}, \text{"near the"}\}. \\ \mathcal{S}^{(\text{INSTRUMENT})} &= \{\text{"with the"}, \text{"using the"}, \text{"by the"}\}. \end{aligned}$$

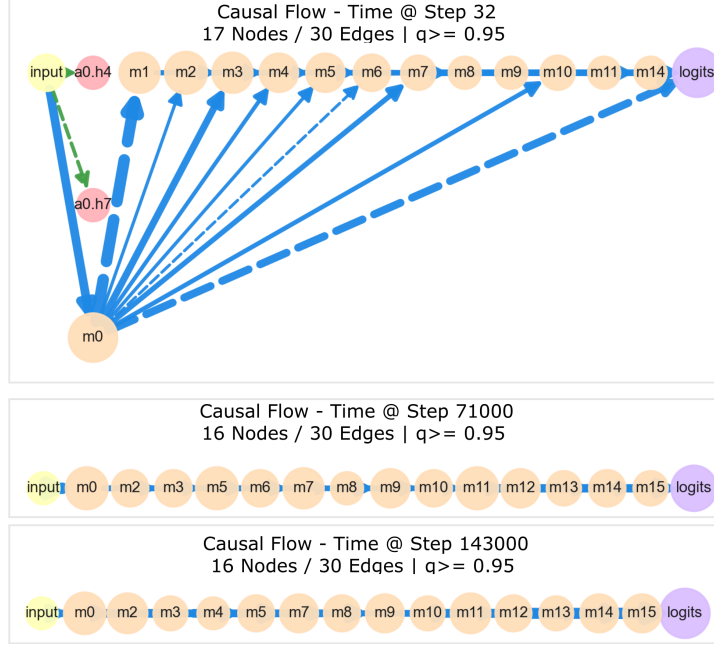


Figure 10: **Developmental trajectory for TIME role across training.** Circuit evolution from initialisation (step 32) through mid-training (step 71000) to convergence (step 143000) demonstrates progressive attention elimination.

We then apply the same filtering criterion as for the main dataset (Section B): we retain only paraphrased prompts $x_{\text{para}}^{(r)}$ for which the model continues to predict the original role-appropriate target $y^{(r)}$ as the most probable next token. This yields a paraphrase set

$$\mathcal{D}_{\text{para}}^{(r)} = \{(x_{\text{para}}^{(r)}, y^{(r)})\} \quad (27)$$

in which all examples are (i) semantically equivalent to the originals at the level of role assignment, (ii) realised with different surface scaffolds, and (iii) correctly handled by the base model.

Circuit consistency evaluation. For each role $r \in \{\text{LOCATION}, \text{INSTRUMENT}\}$, we recompute EAP-IG scores on the paraphrase set and compare them with the original role-cross circuit $\mathcal{C}^{(r)}$ using:

- Top- K node overlap ($K = 20$),
- Edge-weight rank correlation,
- Faithfulness of original circuits on paraphrased prompts.

Summary of control results. Table 13 summarises the results for INSTRUMENT and LOCATION. Across both roles, we observe:

1. **Stable faithfulness under paraphrase:** the original circuits maintain similar causal impact despite scaffold changes (Instrument: +0.02; Location: -0.05).

Table 13: Paraphrase-control evaluation for two roles in PYTHIA-1B. Scores reported for paraphrased inputs at the final training step. Parentheses denote the change relative to the original (non-paraphrased) dataset.

Role	Faithfulness	Top-20 Mass
INSTRUMENT	0.657 (+0.021)	0.925 (+0.009)
LOCATION	0.731 (-0.053)	0.920 (+0.023)

2. **Consistent sparsity structure:** Top-20 mass shifts by less than 0.03 for both roles, indicating that high-importance components remain largely unchanged.
3. **Robust abstraction beyond surface cues:** circuits respond similarly across distinct paraphrastic templates, supporting the interpretation that they encode predicate–argument binding rather than memorised lexical patterns.

These findings reinforce that the circuits identified by our study capture the semantic structure associated with predicate–argument roles, rather than superficial or memorised prepositional cues.

G Method Comparison

We provide a summary comparing mechanistic interpretability methods, along with our choice in Table 14.

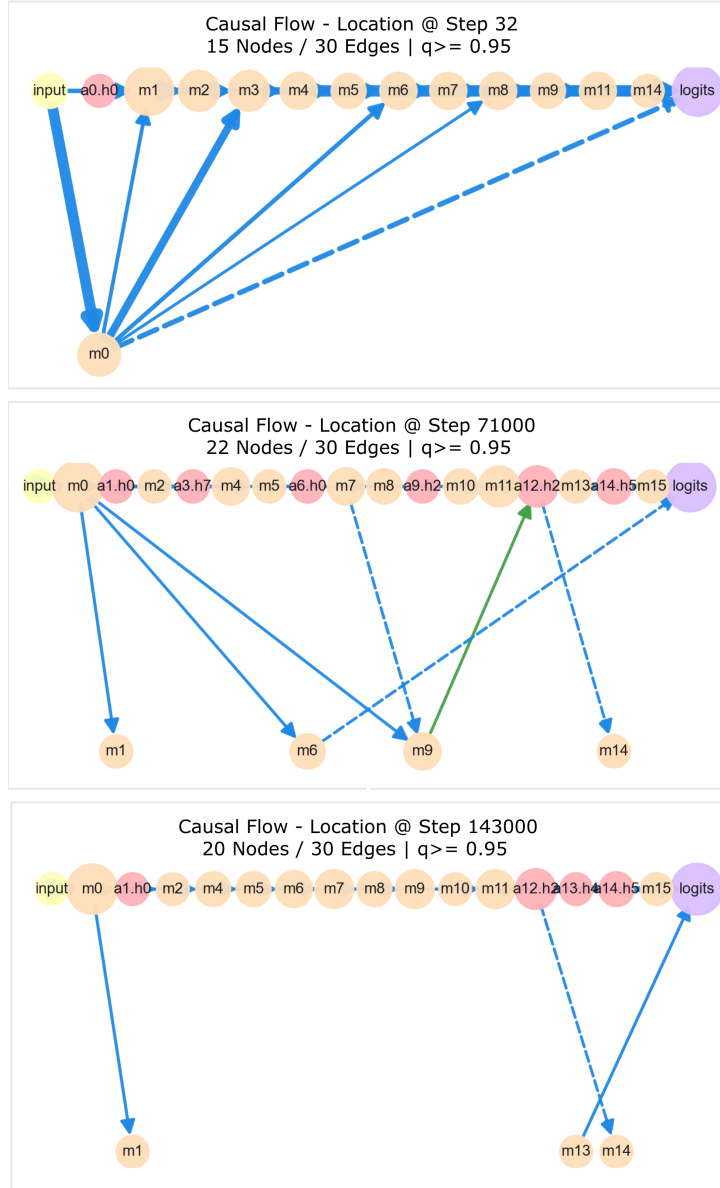


Figure 11: **Developmental trajectory for LOCATION role across training.** Circuit evolution follows an expand then contract pattern with mid-training exploration followed by late-stage pruning.

Method	Faithful	Path-spec.	Granularity	Scalable	Notes / Risks
Linear probing	○	✗	token/residual	✓	Correlational, not causal
Attribution Patching (EAP) (Nanda, 2023; Syed et al., 2024)	○	✓	head/MLP edge	✓	Gradient-based; false negatives
AtP* (Kramár et al., 2024)	✓	✓	head/MLP edge	✓✓	improved faithfulness; residual false negatives
Temporal EAP-IG*	✓	✓	head/MLP edge	✓✓	Baseline/path sensitivity
Path patching (Goldowsky-Dill et al., 2023b)	✓	✓✓	head/MLP path	○	Expensive over checkpoints
Causal scrubbing (Chan et al., 2022)	✓✓	✓✓	hypothesis-level	✗	High implementation cost
SAE (Templeton et al., 2024)	✓	✓	feature-level	○	SAE training; feature drift
Transcoders (Dunefsky et al., 2024)	✓	✓	MLP sublayer	○	Surrogate training; not causal
Circuit tracing / attribution graphs (Ameisen et al., 2025)	○	✓✓	feature-feature	✗	Surrogate fidelity; prompt-specific

Table 14: Comparison of interpretability methods along criteria induced by RQ1/RQ2. ✓✓=strong; ✓=good; ○=partial; ✗=weak.

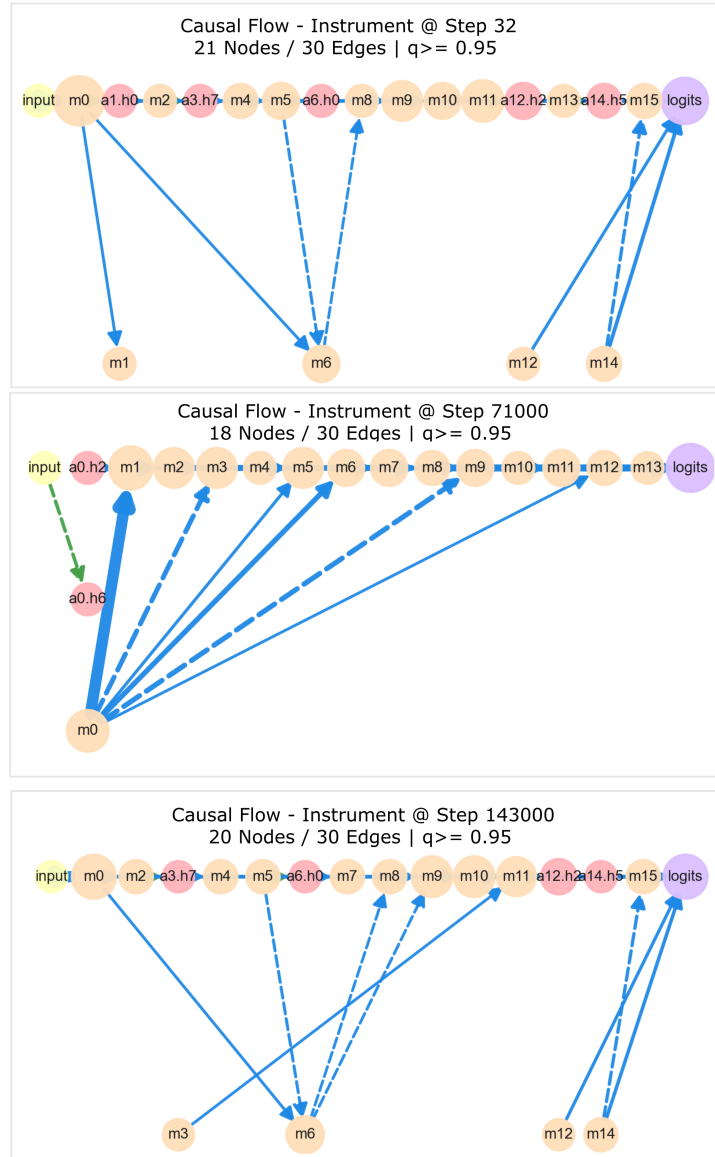


Figure 12: **Developmental trajectory for INSTRUMENT role across training.** Circuit evolution demonstrates stable mid-layer consolidation with minimal late-stage refinement.